Low-level jets' influence on the power conversion efficiency of offshore wind turbines

Johannes Paulsen[1,2], Jörge Schneemann[1,2], Gerald Steinfeld[1,2], Frauke Theuer[1,2], and Martin Kühn[1,2]

[1]Carl von Ossietzky Universität Oldenburg, School of Mathematics and Science, Institute of Physics
[2]ForWind - Center for Wind Energy Research, Küpkersweg 70, 26129 Oldenburg, Germany

Correspondence: Johannes Paulsen (johannes.paulsen@uni-oldenburg.de)

Abstract. Low-level jets (LLJ) are local maxima in the vertical wind speed profile. They are frequently observed at heights of approximately 50 m to 500 m above sea level in offshore regions. The influence of LLJs on the power conversion of the energy flux through the rotor swept area and loads of wind turbines has not ~~been researched thoroughly~~ yet been thoroughly investigated. In this paper we ~~investigate~~ study the influence of LLJs on wind turbines in an offshore wind farm located approximately 15 km from the coast. We derive vertical wind profiles up to heights of 350 m from lidar plan position indicator scans with different elevation angles. We detect LLJs with ~~a frequency of occurrence~~ occurrence rates between 2.4 % ~~to~~ and 22.6 %, based on different definitions used in literature at the observed location. We analyse their influence on the power production of the turbines using operational wind farm data. We observe a negative influence on the power conversion efficiency and increased power fluctuations in LLJ situations compared to situations with equal wind-veer-corrected rotor equivalent wind speed (REWS) but without LLJs. Further, we conduct aeroelastic simulations for a set of wind profiles with varying veer, shear, turbulence intensity and shape of the LLJ core. Comparing situations with the same REWS ~~,~~ revealed that increasing veer and shear both have a negative impact on the simulated power conversion efficiency, while the shape of an LLJ only slightly alters the energy conversion process. Thus, we conclude the main driver for the ~~efficiency-lowering effect~~ lower efficiency during the presence of LLJs to be the combination of positive and negative shear, causing a high absolute shear across the rotor area as well as increased absolute veer.

1 Introduction

The massive expansion of offshore wind power requires an accurate assessment of the available wind resources for existing and future offshore wind projects. Industrial practice typically assumes stability-dependent logarithmic or power law wind profiles as inflow (Lopez-Villalobos et al., 2022). Situations with e.g. high shear or veer as well as local wind speed maxima with a subsequent fall-off towards higher altitudes in the vertical profile, so-called low-level jets (LLJ), are typically not accounted for.

The general phenomenon of LLJ is well known; however, no consensus exists on their definition, detection method and the corresponding site-dependent frequency of occurrence. As occurrences are often found in ~~the height band of the rotor~~heights

between 150 m and 500 m, Emeis (2018) assumes the impact of LLJs on wind ~~turbines - especially offshore -~~ turbine performance — especially offshore — to grow with increasing turbine size.

Different formation mechanisms and types of LLJs have been described in the literature. They occur when one layer of the atmosphere, i.e. the boundary layer, decouples from the friction at the surface and thus experiences an increase in wind speed. This frictional decoupling can be triggered by several processes, e.g. by the sudden change from unstable to stable stratification when crossing the land-sea barrier or in onshore regions during nighttime when the surface temperature decreases due to radiative cooling (Emeis, 2018). Further, LLJs can also emerge during baroclinic situations, as in these cases the thermal wind vector may oppose the direction of the geostrophic wind and thus cause a reverse shear flow (Guest et al., 2018). LLJs are observed to extend to up to 100 km in horizontal direction and last up to multiple hours (Schulz-Stellenfleth et al., 2022). Another type of LLJs are so-called frontal LLJs ~~(FLLJ)~~. This type of LLJ was first reported by Browning and Harrold (1970), describing regions of strong wind speeds travelling ahead of cold fronts. Recently, Baki et al. (2025) showed ~~,~~that these FLLJs, which are followed by a sudden drop in wind speed and strong change in wind direction, can indicate a subsequent downward ramp in power production of offshore wind farms in the Belgian North Sea.

In the literature, ~~several~~ different definitions for an LLJ ~~are used~~can be found. Most are based on either the absolute or the relative fall-off of wind speed between the maximum and the minimum above, or a combination of both (e.g. Kalverla et al., 2019; Rubio et al., 2022; Wagner et al., 2019). The different definitions are applied to adjust the detection to the available measurement methodology and height restrictions. Other studies introduce further criteria, such as specific height bands in which LLJs are expected or a particular relation to the ground-level wind speed (e.g. Ranjha et al., 2013). Further definitions rely on detection based on the characteristics of the wind profile below the jet core (Emeis, 2014). Recently, Hallgren et al. (2023) introduced a new definition particularly intended for wind energy applications, which is based on the local shear around the LLJs' core.

Several studies have been carried out to characterise the frequency of occurrence of LLJs as well as their meteorological characteristics using measurement data. Schulz-Stellenfleth et al. (2022) provide an overview of the meteorological characteristics of LLJs and discuss their possible impacts on offshore wind turbines. However, studies show large differences in the occurrence of LLJs depending on the location and the definition of an LLJ event. Onshore, LLJs were observed in around 20% of all nights at a near coastal location derived from ~~metmast~~ met mast and wind profiler measurements with a maximum height of 1420 m (Baas et al., 2009). At a different location close to Hannover, Germany, where ~~SODAR~~ sodar measurements up to a maximum height of 800 m were available, Emeis (2014) observed LLJs during slightly more than 20 % of all ~~night~~ nights across different weather patterns. Lampert et al. (2016) found LLJs during 52 % of all days close to Brunswick in Northern Germany using ~~lidar~~ light detection and ranging (lidar) measurements reaching altitudes of 500 m. Offshore, LLJs were observed around 11 % of the time at the east-Frisian island Norderney and 7 % of the time at the far offshore island Heligoland using lidar measurements with maximum measurement altitudes of 500 m (Rausch et al., 2022). Pichugina et al. (2017) even detected LLJs in about 63 % of all measured wind profiles in the Gulf of Maine from a measurement campaign in 2004. In this context, it is important to note that none of the before-mentioned locations lie in proximity to nearby wind farms, whose wake effects could alter the wind profile characteristics. The frequency of occurrence of LLJs in offshore conditions strongly

depends on the current season as well as the fetch length and time of the day, with the highest occurrences during wintertime and night (Dörenkämper et al., 2015). Additionally, there are studies based on atmospheric simulations and reanalysis data with a focus on larger areas. Aird et al. (2022) used mesoscale simulations to analyse LLJ characteristics at the east coast of the US and detected LLJs up to a maximum of 12 % of all hours in summer time. Based on ERA-Interim reanalysis data, Ranjha et al. (2013) showed that the occurrence frequency of coastal LLJ events strongly depends on the examined location, climatic zone and the current season. This is further backed up by ?Barekzai et al. (2025b), who showed dependencies of LLJ occurrence frequencies on the present season and wind direction. While Kalverla et al. (2019) pointed out , that the climatological characteristics of LLJs are represented quite well within reanalysis data, they also concluded that speed and height of single events are depicted rather poorly, as they appear smeared out due to the limited vertical resolution of the used models. Similarly, Bui et al. (2025) demonstrate that LLJ intensity is often underestimated by reanalysis data, by comparing them to lidar measurements gathered at the FINO1 offshore platform in the German North Sea. Kalverla et al. (2019) further noted, that LLJs should be regarded in the parametrisation of wind profiles to reduce uncertainties in the performance prediction of offshore wind farms.

The impact of LLJs on the performance of offshore wind turbines is investigated by other studies using numerical methods. When analysing the power production and turbine loads, it is crucial which reference wind speed and atmospheric stability regime is applied for the comparison between different wind profile conditions. This, however, is not consistent in the existing literature, as here hub height wind speeds (e.g. Gadde and Stevens, 2021) or the rotor equivalent wind speed (e.g. Zhang et al., 2019) are not comparable between the different cases examined in the studies. Gadde and Stevens (2021) studied the influence of LLJs on the power output of wind turbines using large-eddy simulations (LES). As the LLJs' core height and atmospheric stratification are controlled via the surface cooling rate, but the geostrophic wind speed is kept constant, the hub height wind speeds as well as the rotor equivalent wind speeds differ between the different cases. Gadde and Stevens (2021) found a positive influence of the simulated LLJs on the turbines' power production during free inflow, compared to non-LLJ situations, as the entrained energy in the wind is increased due to the LLJs' presence. Further, they observed improved wake recovery for the first five to six turbine rows in a wind farm during a stable boundary layer with LLJ events present, compared to a turbulent neutral boundary layer. For the rows of turbines in the rear part of the wind farm, wake recovery is influenced negatively in stably stratified conditions with LLJs present. On the other hand, Zhang et al. (2019) reported from aeroelastic simulations , that turbines perform worse during LLJ events compared to situations with logarithmic wind profiles with the same hub height wind speed. In a different another study, Schepers et al. (2021) derived highly resolved wind fields for aeroelastic simulations from LES simulations driven by mesoscale simulations representative for one year. Subsequently, they investigated the loads experienced during an exemplary LLJ with a core approximately at hub height and four extreme meteorological events for a comparison with the design load cases. Applying simulations with blade-element momentum theory and a free vortex wake model of a 10 MW offshore turbine, the authors observed a decrease in damage equivalent and extreme blade root flapwise bending moments during the presence of the LLJ compared to design conditions. They attributed this decrease in experienced loads partly to the lower turbulence intensity observed during LLJs, and partly to the "non-extreme" shear compared to the observed design load cases defined by the International Electrotechnical Commission (IEC). Similarly, Gutierrez et al. (2017)

observed decreases in tower and nacelle motions from aeroelastic simulations, when turbines are exposed to negative wind shear above the LLJ core, with increasing benefits, the more of the rotor area is covered by the negative shear profile.

During a two-month-long onshore campaign using Doppler wind lidar data, Weide Luiz and Fiedler (2022) showed that nocturnal LLJs shift the mean wind speed at hub height to higher values, compared to nights without LLJs present. The authors concluded that LLJs increase the average power production. However, the authors also reported that increased shear across the rotor area negatively impacts the turbines' power production. Further, their study mainly focused on probability distributions and mean values, instead of providing a comparison between LLJ and non-LLJ situations with the same hub height wind speeds or the same rotor equivalent wind speeds. Roy et al. (2022) used ~~metmast~~ met mast data and machine learning methods to detect and characterise LLJ events. The authors analysed the power production during nocturnal LLJ and non-LLJ conditions without comparing situations with corresponding wind speeds, but showing overall increased wind speeds during LLJ events. Murphy et al. (2020) report about impacts of high shear and veer events, also present during LLJ events, on wind turbine power production at an onshore location in the North American plains. The authors found a negligible influence of the shear exponent, while a high total directional veer across the rotor area coincides with decreased power production. Also, they showed that during these events, large differences between hub height wind speed and rotor equivalent wind speed (REWS) lead to discrepancies in the observed power production.

In summary, many studies analysed the occurrence and characterisation of LLJs. Also, using numerical studies, the importance of shear and veer and the presence on LLJs on turbine power performance and loads has been assessed. However, experimental insight into the influence of LLJs on the performance of commercially operating offshore wind turbines, including the systematic analysis of operational data of several turbines, concerning the produced power and experienced loads, is largely missing. Also, the application of different LLJ definitions makes the comparison of existing studies very difficult. Further, the way LLJ profiles are compared to reference inflow cases is not consistent in the literature. While some studies compare inflow situations with similar hub height wind speeds, others generate LLJs with a similar ratio of the core speed to the geostrophic wind speed by varying the surface cooling rate. Thus, the energy contained within the wind over the rotor swept area is not comparable between LLJ and non-LLJ situations. Therefore, more detailed research on LLJ occurrence and their impact on wind turbines, compared to situations with stability corrected logarithmic wind profiles with equal REWS, is necessary for a refined wind resource assessment and understanding of wind turbine operation. This is especially important for upcoming turbine generations with even larger rotor diameters.

The objective of this study is to experimentally and numerically assess the impact of LLJs on the power conversion efficiency of offshore wind turbines. To achieve this goal we derive vertical wind profiles from lidar measurements, estimate the atmospheric stability from local meteorological measurements and analyse the occurrence frequency and characteristics of LLJs at an offshore wind farm. Here, we first compare the different definitions, before focussing on the shear-based LLJ definition introduced by Hallgren et al. (2023). Subsequently, the conversion efficiency of the offshore wind turbines is analysed by investigating operational data and comparing situations with and without LLJs with the same rotor equivalent wind speed (REWS), ensuring the same energy flux through the rotor area. To further deepen our understanding of the underlying processes we carry out ~~aeroelastical simulations of~~ aeroelastic simulations providing different LLJ profiles as inflow conditions.

This paper consists of five main sections. Following the introduction, Section 2 introduces the applied methodology. Section 3 shows the results of the study, followed by a discussion in Section 4 and a brief conclusion including an outlook for future research in Section 5. Further, the methodology for the atmospheric stability assessment in a near coastal region is elaborated on in Appendix A. Appendix B provides the calculations, on which the uncertainty estimation of the rotor equivalent wind speed is based on. For a basic assessment of the applicability of the approach of vertical wind profile generation used in this study, we provide a comparative study between profiles generated from the entire measurement volume of the lidar scanned sector to more localised wind profiles in Appendix C.

2 Methods

This section describes the measurement site and methodology (Sect. 2.1), the processing of the lidar data and wind profile generation (Sect. 2.2), the detection of LLJs (Sect. 2.3) and the process of analysing the influence of LLJs on offshore wind turbine performance (Sect. 2.4).

2.1 Measurement campaign at the offshore wind farm Nordergründe

The lidar data we use for this study are obtained from a measurement campaign at the Nordergründe (NG) wind farm in the German Bight from October 2021 to September 2022. Figure 1a ~~provides~~ indicates the position of the measurement site together with the ~~deployed wind farms~~ wind farms installed in the German North Sea ~~as of~~ at the time of the measurement campaign. The wind farm is located near the coast with the closest distance to the German mainland being 15 km in south-westerly direction. The farm features 18 bottom-fixed turbines of the type Senvion 6.2M126 with a rotor diameter $D = 126\,\mathrm{m}$, a hub height $z_{\mathrm{hh}} = 84\,\mathrm{m}$ above mean sea level (MSL), a rated wind speed $v_{\mathrm{r}} = 14\,\mathrm{ms}^{-1}$ and a rated power $P_{\mathrm{r}} = 6.15\,\mathrm{MW}$. We use data from the long-range scanning lidar Vaisala Windcube 400S (serial no. 192), which was installed on the transition piece (TP) of turbine NG17, roughly 16.5 m above MSL. The turbine NG17 is located at the south-western corner of the wind farm and thus experiences free inflow for south-easterly to north-westerly wind directions (Fig. 1b). The measurement campaign was initially designed with the goal to improve minute-scale wind and power forecasting methodologies (Theuer et al., 2024), but proved useful for LLJ detection and characterisation.

The lidar at NG17 ~~measures~~ measured a set of azimuthal scans (plan-position indicator, PPI) with increasing elevations, similar to Goit et al. (2020) and Visich and Conan (2025). The measurement sector is aligned with the prevailing wind direction at lidar height according to Theuer et al. (2024) and each PPI covers an azimuthal range, i.e. has an opening angle, of 80°. For each azimuthal angle, the lidar is able to process wind speed information at 159 ranges along the beam, also called range gates. ~~At~~ For each range gate, the line-of-sight velocity v_{LOS} and carrier-to-noise ratio (CNR) as a quality measure are stored. One set of 16 consecutive PPI scans with increasing elevation takes around 75 s to finish, including the measurement reset time after each consecutive PPI scan. The first scan is measured with a negative elevation angle of -0.2°, followed by 15 scans with elevations ranging from 0° to 2.1° in steps of 0.15°. Table 1 provides more details of the scanning characteristics and Fig. 2a depicts a vertical slice of the scanning pattern including the rotor swept area and lidar positioning on the TP 16.5 m above

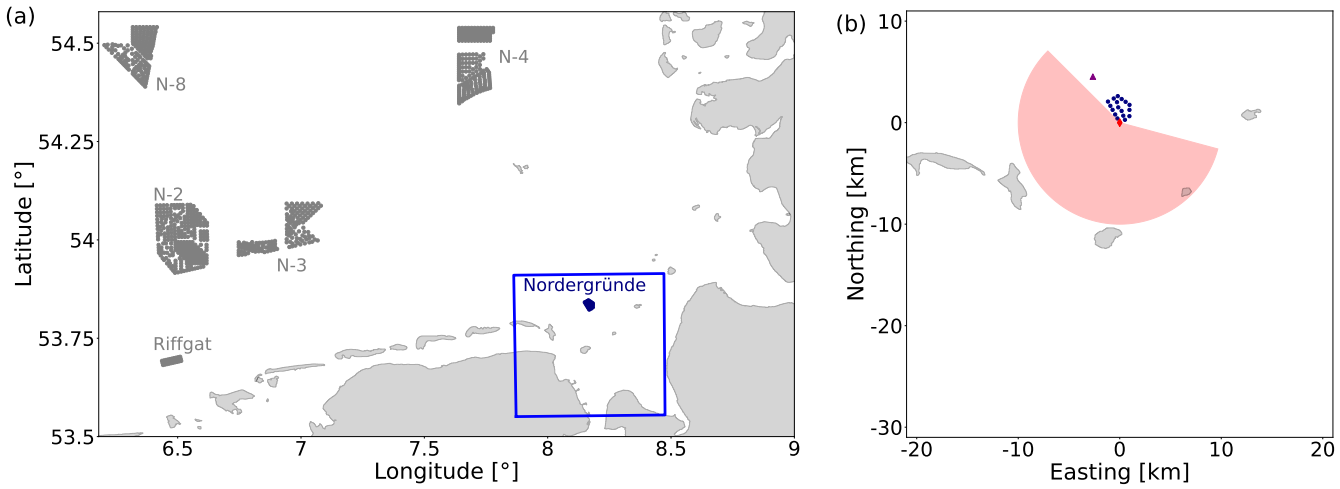

Figure 1. (a) Overview of the German North Sea with operational German offshore wind farms, as of the time of the end of our study (October 2022), depicted in grey. The wind farm Nordergründe where the measurements were conducted, is marked in blue. (b) Layout of NG, also including the nearby coastline (blue square in (a)). The unobstructed lidar scan sector is marked in red. Further, the position of the lighthouse Alte Weser is depicted (purple ▲).

mean sea level. Further, the lidar ~~also was~~ was also equipped with two inclination sensors (Micro-Epsilon INC5701), which measure the pitch and roll movement of the lidar in a resolution of 2 Hz.

Table 1. Details about the scan settings of the lidar mounted on turbine NG17. Elevation angles and range gates are listed as minimal value : spacing : maximal value.

Lidar height (MSL) [m]	16.5
Visible lidar sector for free inflow at NG17 [°]	105 to 315
PPI opening angle [°]	80
Azimuthal resolution [°]	2
Scanning speed (azimuthal direction) [°/s]	20
Elevation angles [°]	-0.2 ~~,~~and 0 : 0.15 : 2.1
Accumulation time [ms]	100
Range gates [m]	300 : 60 : 9780

Meteorological measurements are available at the wind turbine NG17. We use a Vaisala HMP155 sensor to measure air temperature and humidity and a Vaisala PTB330 to measure air pressure. Both sensors are installed near the lidar system at 16.5 m above MSL and provide measurements at a frequency of 1 Hz. To assess the sea-surface temperature (SST) we use a system of two infrared (IR) sensors Heitronics CT09 and CT15, measuring at a resolution of 1 Hz, which apply an internal correction for sky radiation. As this system was only installed in April 2022, we use a water temperature measurement at the

lighthouse Alte Weser, providing data in one minute intervals, for the previous period. Further information on the SST and water temperature measurements is found in Appendix A. Table 2 shows the available periods of the different data sources. The meteorological measurements are used to estimate the prevailing stability regime at the measurement location, via the Obukhov length L following Schneemann et al. (2021). First, the bulk Richardson number

$$Ri_b = \frac{g}{T_\mathrm{v}} \frac{0.5 z_\mathrm{TP} \left(\Theta_\mathrm{TP} - \Theta_0\right)}{u_\mathrm{li}^2} \tag{1}$$

is calculated using the gravitational acceleration g, the virtual temperature at the sea surface T_v, the transition piece height z_TP, the virtual potential temperatures at transition piece height and sea surface Θ_TP and Θ_0, respectively, and the wind speed at transition piece height as measured at the closest range gate of the lidar u_li. Second, the bulk Richardson number is used to compute the dimensionless stability parameter

$$\zeta = \begin{cases} \frac{10 Ri_b}{1 - 5 Ri_b} & Ri_b > 0 \\ 10 Ri_b & Ri_b \leq 0. \end{cases} \tag{2}$$

Finally, we compute the Obukhov length

$$L = \frac{0.5 z_\mathrm{TP}}{\zeta}. \tag{3}$$

Due to our measurements of meteorological parameters at sea surface level and transition piece height, the estimation of L is strictly valid only between these two heights.

Table 2. Overview of used data for atmospheric stability estimates. The data from the Alte Weser lighthouse is publicly available at WSV (2023).

Quantity	Symbol	Location	Sensor	Usage period
Air temperature	T_air	TP NG17	HMP155	01/10/2021 - 30/09/2022
Relative humidity	Φ	TP NG17	HMP155	01/10/2021 - 30/09/2022
Air pressure	p_air	TP NG17	PTB330	01/10/2021 - 30/09/2022
Wind speed	v_LOS	TP NG17	Windcube 400S	01/10/2021 - 30/09/2022
Sea surface temperature	$T_\mathrm{SST,\,NG17}$	NG17	Heitronics CT09/CT15	01/04/2022 - 30/09/2022
Water temperature	$T_\mathrm{AlteWeser}$	Alte Weser lighthouse	WTW TetraCon 700 IQ SW	01/10/2021 - 31/03/2022

2.2 Lidar data processing and wind profile generation

Lidar data processing consists of the three main steps data quality control and filtering, wind direction assessment and exclusion of lidar beams almost perpendicular to the wind direction. First, we filter the data using a predefined quality flag provided by the lidar manufacturer mainly based on the carrier-to-noise ratio of the measurements as well as a range availability filter. ~~Second~~Secondly, applying the velocity azimuth display (VAD) algorithm the horizontal wind speed is computed from the

measured line-of-sight velocities v_{LOS} (Werner, 2005). Here, we assume a spatially homogeneous average wind direction across each range gate and a negligible influence of the vertical wind speed component due to the small elevation angles. To obtain the wind direction at each range gate, we perform a least-squares fit using a cosine-function to fit the measured v_{LOS}. The phase offset of the obtained fit determines the wind direction for the particular subset of the data. Next, the horizontal wind speed v_{hor} can be computed as

$$v_{\mathrm{hor}}(\theta, r) = \frac{v_{\mathrm{LOS}}}{\cos(\theta - \chi(r))\cos(\alpha)} \tag{4}$$

with the azimuth angle θ, the wind direction $\chi(r)$ at each range r and the elevation angle α.

Third, measurements gathered at azimuth angles approximately perpendicular to the mean wind direction, i.e.

$$75^\circ < |\theta - \chi| < 105^\circ \tag{5}$$

are removed from the analysis~~, due to the high uncertainty associated with these measurements~~. Due to the very small wind component in the direction of the line of sight of the lidar the uncertainty in the reconstructed main wind component is high at these angles, as the relative error of the measurement itself, as well the impact of the wind component perpendicular to the main wind direction are increased. Further, we ~~exclude scans recorded from north-easterly wind directions, i.e. between wind directions of~~ do not consider scans recorded in the wind direction sector from 320° ~~and~~ to 100° to ~~filter out~~ exclude measurements of the wind farm wake, which could lead to false detections of LLJ events in the further analysis.

For the lidar measurements, several uncertainties regarding the tilt of the lidar due to the turbine movement and the earth's curvature are introduced during the measurement process (Schneemann et al., 2021). First, there are uncertainties regarding the pitch and roll angles of the lidar which dynamically change due to platform movement of the TP, which is mainly caused by the thrust of the wind turbine rotor (Rott et al., 2022). To account for this, we use tilt measurements of inclinometers placed in the lidar and we correct the height of the lidar probe volume. During periods without inclinometer measurements, we use a different method introduced by Rott et al. (2022). ~~).~~ This method estimates the platform tilt without any motion sensor measurements and instead relies on the yaw position and power production of the turbine. ~~Second~~Secondly, a systematic variation of the measurement height above mean sea level is introduced due to the earth's curvature. We account for this variation by correcting the height of all measurements according to Osterman (2012). Note that variations of the water surface elevations with respect to mean sea level to the tides (tidal range approx. 3 m) or other meteorological conditions are not considered.

To derive vertical wind profiles from the preprocessed lidar data, the ~~computed~~ horizontal wind speeds computed from the lidar PPI scans with different elevation angles are ~~averaged spatially for~~ sorted in different height bands with a vertical resolution of 10 m~~. Spatial averaging in this case incorporates~~ , spanning over the complete measurement range of the lidar from 300 m to 9780 m ~~,~~and across the entire azimuth sector of the scan.

~~Following the generation of the vertical wind profiles, the data from different scans is resampled to~~ The horizontal wind speeds and directions in each height band are averaged on 10-minute ~~intervals by averaging the wind speeds and taking the vector average~~ intervals.

Next, low-quality profiles, with large data gaps or an extremely high average wind shear and as well as a high standard deviation of the wind ~~directions at their respective heights~~shear are excluded. Further, the wind profiles are slightly smoothed using a rolling average with a window size of 30 m.

As we are interested in LLJ phenomena, which are present on spatial scales encompassing the entire wind farm and temporal scales of 10 minutes, this spatial averaging reduces noise in the data, i.e. short term and small scale turbulent fluctuations in the wind field. This allows for a more robust detection of persistent LLJs. To analyse the robustness of our applied method against a more localised analysis, we compare the spatially averaged profiles to more localised wind profiles derived from the same lidar scans using a method similar to Visich and Conan (2025) in Appendix C.

2.3 LLJ definition and detection

Figure 2b shows an exemplary depiction of a wind profile containing an LLJ. Here, important nomenclature, such as the core speed and core height of the jet, i.e. the maximum wind speed and the height at which it occurs are illustrated. The fall-off for this particular jet is depicted as well. For reference, a logarithmic wind profile with the same REWS is displayed.

We detect LLJs from 10-minute average lidar wind profiles and use different LLJ definitions found in the literature (Table 3). Except for one definition, all use the wind speed fall-off for LLJ characterisation. The definition used by Ranjha et al. (2013) introduces the core height and relation to the wind speed at the lowest available height as further thresholds. In contrast to this, Hallgren et al. (2023) chose to define an LLJ event based on the maximum shear above and below the jet core.

Table 3. Different LLJ definitions applied in this study.

Defined by	Criteria (Conjunctive)
Hallgren et al. (2023)	• Shear above ~~above~~ core height $\leq -0.01\,\mathrm{s}^{-1}$ • Shear below the core $\geq 0.01\,\mathrm{s}^{-1}$
Kalverla et al. (2019)	• Absolute fall-off $\geq 2\,\mathrm{ms}^{-1}$
Ranjha et al. (2013)	• Relative fall-off $\geq 20\,\%$ • Core wind speed at least $20\,\%$ higher than wind speed at lowest available model or measurement height • Core height below $2\,\mathrm{km}$
Rubio et al. (2022)	• Absolute fall-off $\geq 1\,\mathrm{ms}^{-1}$
Wagner et al. (2019)	• Absolute fall-off $\geq 2\,\mathrm{ms}^{-1}$ • Relative fall-off $\geq 25\,\%$

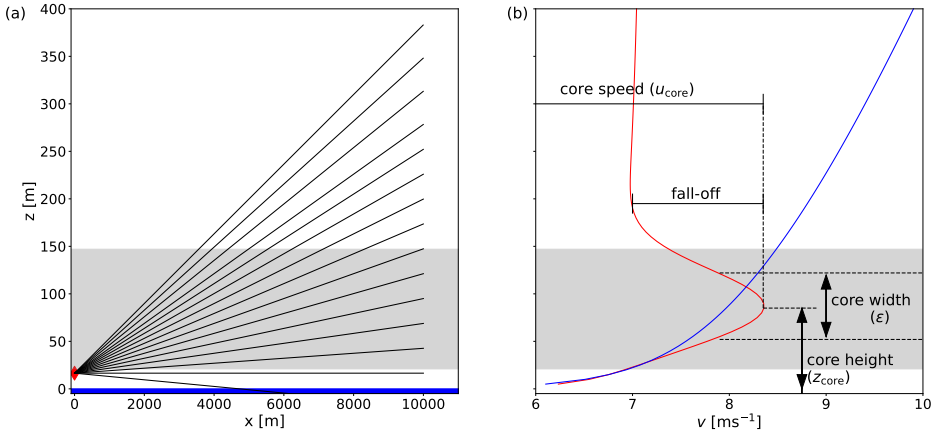

Figure 2. (a) Exemplary scanning pattern for the lidar measurement campaign, with the position of the lidar displayed at the height of the transition piece (red ♦), the lidar beams as black lines and the height range of the rotor swept area marked as a gray background. (b) Exemplary LLJ profile in red, with the important terminology defined. For reference, a logarithmic wind profile with the same REWS of $8\,\mathrm{ms}^{-1}$ is shown in blue.

By applying the described LLJ definitions we systematically analyse the gathered wind profiles for the occurrence of LLJs within the given time frame.

2.4 Wind turbine performance analysis via an equal REWS framework

To investigate the performance of offshore wind turbines under the influence of LLJs, we calculate wind turbine power curves from lidar based REWS and compare them in LLJ and non-LLJ situations. Therefore, we use operational data of the wind farm Nordergründe. The data from the Supervisory Control and Data Acquisition (SCADA) system contains various parameters that describe the turbine condition, such as the generated power, the yaw direction, blade pitch and operational status as well as meteorological parameters derived at hub height, i.e. wind speed and direction. We choose turbines in undisturbed inflow for a south-easterly to north-westerly wind direction sector. Subsequently, we filter the SCADA data for the different turbines with respect to the wind directions to only include data featuring undisturbed inflow (Figure 3). For the first row facing in south-westerly direction (green ■ in Fig. 3), the included sector spans from 185° to 315° and for the first row facing in south-easterly direction (magenta ♦ in Fig. 3) the sector spans from 105° to 190°. As NG17 is located at the south-westerly corner it is included in the analysis of both sectors.

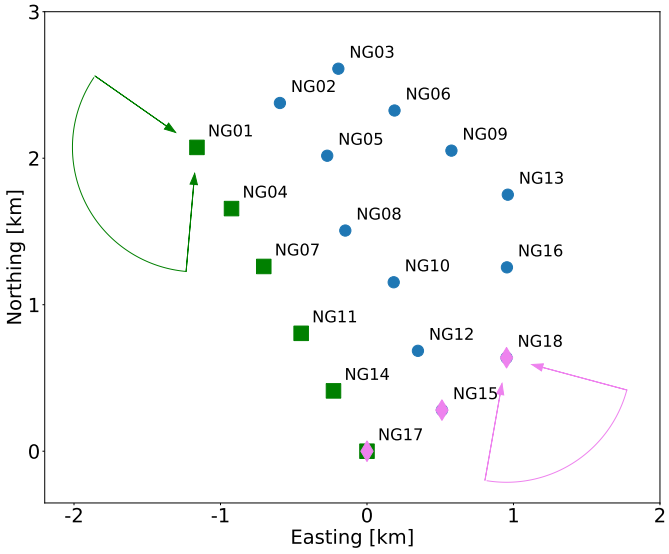

Figure 3. Layout of wind farm NG with turbine names. The turbines selected for further analysis are marked in green and magenta respectively and their corresponding wind direction sectors are specified as arrows with matching colours.

We use SCADA data of the turbines with a resolution of 0.2 Hz. First, we filter the data according to the wind turbine's operational status, such that cut-in, breaking and curtailment situations are not considered. Further, situations where the turbines are not operating at their optimal operating points, e.g. when the yaw angle of the nacelle is misaligned with respect to the wind direction measured by the lidar by more than 45° or the blade pitch exceeds 20 °, are discarded. Subsequently, the operational data is resampled to 10-minute averages. In addition to the mean apparent power μ_P we also quantify the normalised power fluctuations, i.e. power turbulence intensity ($\mathrm{PO_{TI}}$) similar to the turbulence intensity (TI) in the wind speed as

$$\mathrm{PO_{TI}} = \frac{\sigma_P}{\mu_P} \tag{6}$$

using the standard deviation of the apparent power σ_P normalised by the mean apparent power μ_P (Mittelmeier et al., 2017).

Next, the data is filtered for LLJ situations, where only LLJs with a core height between the upper and lower tip of the rotor are included.

Subsequently, the rotor equivalent wind speed (REWS) is calculated from the wind profiles derived in Section 2.2. We use the REWS to estimate the flux of kinetic energy through the rotor-swept area under consideration of wind veer as done in power performance measurements according to IEC 61400-12-1 (IEC, 2017). This is more meaningful than a simple wind speed measurement at hub height when analysing the power output of a wind turbine, as it also considers the wind shear across the swept area. Figure 4 shows exemplary wind speed and direction profiles stressing the importance to include wind veer in the analysis.

To begin with, we perform a density correction of the measured wind speed as done in power performance measurements according to IEC 61400-12-1 (IEC, 2017). To this end, we first compute the air pressure p at different heights z as in

$$p(z) = p_0 \left(1 + \frac{\Gamma}{T_0}(z - z_{\mathrm{TP}})\right)^{-\frac{g}{L R_0}} \tag{7}$$

with the air pressure and temperature at TP height p_0 and T_0, the lapse rate $\Gamma = 6.5\,\mathrm{K\,km^{-1}}$, the TP height z_{TP}, the gravitational acceleration $g = 9.81\,\mathrm{ms^{-2}}$, the Obukhov length L and the universal gas constant for dry air $R_0 = 287.05\,\mathrm{J\,kg^{-1}\,K^{-1}}$. Secondly, we extrapolate the measured temperatures to the desired height via

$$T(z) = T_0 - \Gamma(z - z_{\mathrm{TP}}). \tag{8}$$

Third, we compute the density

$$\rho(z) = \frac{1}{T(z)} \left(\frac{p(z)}{R_0} - \Phi(z) P_{\mathrm{W}} \left(\frac{1}{R_0} - \frac{1}{R_{\mathrm{W}}}\right)\right) \tag{9}$$

with the relative humidity $\Phi(z)$, the vapour pressure $P_{\mathrm{W}} = 2.05 \cdot 10^{-5} \exp(0.06312\ T_0)\,\mathrm{Pa}$ and the gas constant of water vapour $R_{\mathrm{W}} = 461\,\mathrm{J\,kg^{-1}\,K^{-1}}$. Finally, the density-corrected wind speed

$$v_{\mathrm{corr}}(z) = v(z) \left(\frac{\rho(z)}{\rho_0}\right)^{1/3} \tag{10}$$

is calculated with the standard air density $\rho_0 = 1.225\,\mathrm{kg\,m^{-3}}$.

Subsequently, we calculate the REWS

$$v_{\mathrm{eq}} = \left(\sum_{i=1}^{n_h} \left(v_{i,\mathrm{corr}} \cdot \cos(\phi_i)\right)^3 \frac{A_i}{A}\right)^{1/3} \tag{11}$$

with the total number of chosen height sections n_h, the density corrected wind speed in the i-th height segment $v_{i,\mathrm{corr}}$, the difference between hub height wind direction and wind direction within the i-th segment ϕ_i, the area of the i-th segment A_i, and the total rotor swept area A. The ~~different segments are spanned~~ segments span around each of the 13 measurement heights of the wind profile within the rotor area. Thus, the REWS is computed from 13 wind speeds and directions across the rotor plane.

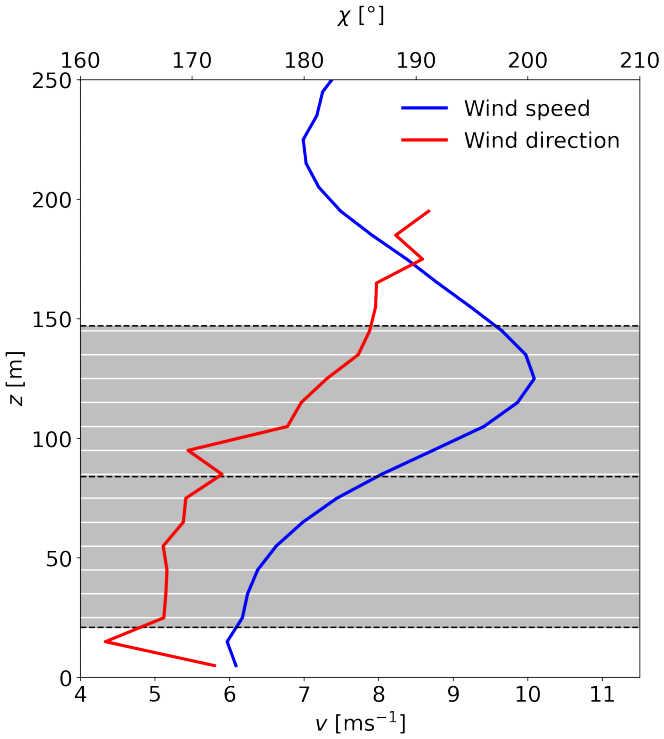

Figure 4. Exemplary measurement of a vertical wind speed profile (blue) and direction profile (red). Additionally, the lower tip, upper tip and hub height of the turbine are represented as dashed lines and the segments used for the determination of the REWS are shaded in grey.

Further, we also computed an uncertainty estimation for the REWS Δv_{eq} at each individual timestamp, which is further elaborated on in Appendix B.

Finally, we generate a power curve following the IEC 61400-12-1 (IEC, 2017), by classifying the data into wind speed bins based on the REWS of $0.5\,\mathrm{ms}^{-1}$ and averaging the apparent power obtained from SCADA within each bin. Here, only bins containing at least 30 minutes (i.e. 3 different 10 minute averaged measurements) of data are considered. We generate an uncertainty interval around this first power curve, by adding and subtracting Δv_{eq} from the the measured time series and repeating the power curve calculation. While following the IEC 61400-12-1 (IEC, 2017) in most parts, the power curves generated for this study are not fully compatible with the standard. Other criteria, such as e.g. measuring the vertical wind profile two to four rotor diameters in front of the turbine are not met.

2.5 Aeroelastic simulation of LLJ events

To support our experimental analysis we perform aeroelastic simulations with ~~openFAST~~ OpenFAST v3.5.0 to compare the energy conversion process during LLJ and non-LLJ situations (National Renewable Energy Laboratory, 2023). As a basis for these simulations we define 156 different vertical wind profiles, each with different combinations of veer, shear, Obukhov length L and ~~turbulence intensity~~ TI. The different quantities varied for the respective profiles are portrayed in Table 4. We

include 12 uniform inflow profiles with varied veer and TI, 36 logarithmic wind profiles with different veer, shear and TI and 108 wind profiles including LLJs with varying veer, TI, core height and core ~~widths~~width. While a maximum veer across the rotor area ($\Delta\Theta$) of 40° ~~seem~~ seems to be large even for stable conditions, these extreme events are present in our own measurements as well as observed in the literature (e.g. Olsen et al., 2025; Murphy et al., 2020).

We compute stability corrected logarithmic wind profiles

$$v_{\log}(z) = \sqrt{\frac{z_0 g}{\alpha_c}} \frac{1}{\kappa} \left(\ln\left(\frac{z}{z_0}\right) - \Psi\left(\frac{z}{L}\right) \right) \tag{12}$$

following Schneemann et al. (2021) with the height z, the gravitational constant $g = 9.81\,\mathrm{ms}^{-2}$, the von Kárman constant $\kappa = 0.4$, the Charnock parameter for offshore environments $\alpha_c = 0.011$ and the stability correction term

$$\Psi = \begin{cases} 2\ln\left(\frac{1+x}{2}\right) + \left(\frac{1+x^2}{2}\right) - 2\arctan(x) + \frac{\pi}{2} & \text{, for } L < 0 \\ -\beta\frac{z}{L} & \text{, for } L \geq 0 \end{cases} \tag{13}$$

where $x = \left(1 - \gamma\frac{z}{L}\right)^{1/4}$, γ = 19.3 and β = 6.

To incorporate LLJs into this definition, we added a Gaussian Bell curve

$$v_{\mathrm{LLJ}}(z) = \mathrm{SF} \cdot \frac{1}{\varepsilon\sqrt{2\pi}} \exp\left(\frac{1}{2} \left(\frac{z - z_{\mathrm{core}}}{\varepsilon} \right)^2 \right) \tag{14}$$

with an empirical scaling factor SF = 200 $\mathrm{m}^2\mathrm{s}^{-1}$ to control the strength of the LLJ, the desired core height z_{core} and the core width of the LLJ ε. For all LLJ profiles, we choose unstable atmospheric conditions with L = -100 m, to keep the shear outside of the jet core as low as possible and isolate the effects of the jet core from other shear related effects.

To ensure similar energy flux through the rotor for all different simulations we compute the REWS v_{eq} for every profile and subsequently normalise to a REWS $v_{\mathrm{eq,\,ref}} = 8\,\mathrm{ms}^{-1}$. Thus in total, the LLJ profiles are designed as

$$v(z) = (v_{\log}(z, L) + v_{\mathrm{LLJ}}(z, SF, z_{\mathrm{core}}, \varepsilon)) \cdot \frac{v_{\mathrm{eq}}}{v_{\mathrm{eq,\,ref}}}. \tag{15}$$

Similarly, the logarithmic and uniform wind profiles are normalised to a wind veer-corrected REWS $v_{\mathrm{eq,\,ref}} = 8\,\mathrm{ms}^{-1}$.

Figure 5 shows exemplary profiles used for the aeroelastic simulations.

Table 4. Parameters for the generation of artificial wind profiles used to simulate the turbine response in ~~open~~FAST~~FAST~~OpenFAST. The varied parameters include the turbulence intensity (TI), veer across the rotor area ($\Delta\Theta$), Obukhov length (L), core height (z_{core}) and core width (ε).

Profile shape	TI [%]	$\Delta\Theta$ [°]	L [m]	z_{core} [m]	ε [m]
Uniform	0, 5, 10	0, 10, 20, 40	/	/	/
Logarithmic	0, 5, 10	0, 10, 20, 40	-100, 100, 1000	/	/
LLJ	0, 5, 10	0, 10, 20, 40	-100	27, 85, 143	20, 40, 60

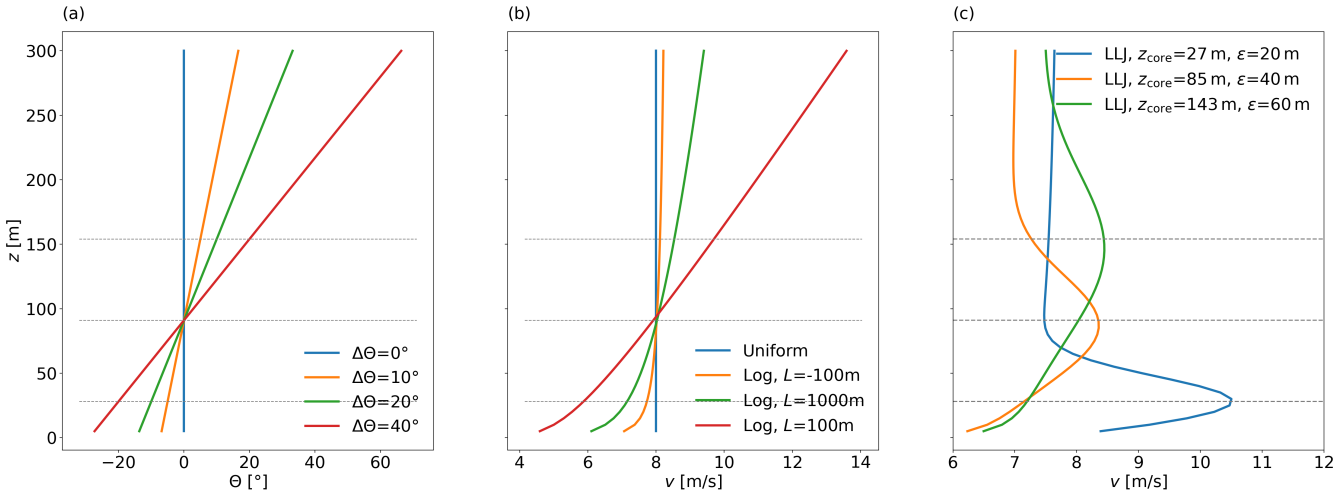

Figure 5. Exemplary inflow profiles used for the aeroelastic simulations normalised to $v_{\mathrm{eq}} = 8\,\mathrm{ms}^{-1}$. (a) provides the used wind direction profiles for all the different wind speed profiles, while (b) shows exemplary uniform and logarithmic profiles. In (c) exemplary LLJ profiles with different core heights and core widths are shown.

Using TurbSim (Jonkman and Buhl, 2005), we generate three-dimensional wind fields (width, height and time) containing all three wind speed components for each combination of employed wind speed and direction profiles.

We use the NREL-5MW reference turbine (Jonkman et al., 2009) in our simulations, as it features similar dimensions as the Senvion 6.2M126 turbines installed at NG. We include a model of the turbine installed on a monopile without hydrodynamic loading and use a simulation time of 600 s with time steps $dt = 0.005\,\mathrm{s}$. To exclude artefacts from the initialisation process, we remove the first 100 s from our simulation. Further, structural dynamics (ElastoDyn), sub-structural dynamics (SubDyn), control and electrical-drive dynamics (ServoDyn) as well as aerodynamic loads (AeroDyn) are computed using different sub-routines within the ~~openFast~~ OpenFAST framework.

3 Results

In this section, we characterise the observed LLJs at the offshore wind farm Nordergründe (Section 3.1) and compare the apparent power production of the wind turbines during situations with the same REWS with and without LLJs present (Section 3.2) as well as the fluctuation in the power production (Section 3.3). Further, we analyse the aeroelastic simulations of the turbines with and without LLJ events present and show the change in turbine performance during LLJ events (Section 3.4).

3.1 Characterisation of LLJ events

To begin our analysis, we evaluate the occurrence statistics of LLJ events at the NG wind farm. For the characterisation of this location all detected LLJs independent of their core height are included. After excluding measurements with ~~insufficient data quality or~~ wind farm wakes inside the lidar scanned area (approx. 27 % of the data) or insufficient data quality (approx. 3 %

of the data), we apply the LLJ detection algorithm. Following all these steps 30,698 10-minute intervals remain, amounting to 5,116.33 h of available data. The availability at the highest altitudes is quite good, given the fewer measurement points in these regions, with over 30 % of all considered profiles reaching heights over 340 m. More than 66 % of all profiles contain data at altitudes larger than 250 m and more than 85 % of all profiles contain data up to 150 m, thus spanning the entire rotor swept area.

Table 5 shows the amount of time we detect LLJs in the lidar wind profiles based on the different definitions applied in this study. Using the definition adapted from Rubio et al. (2022) we observe a relatively high value with LLJs present at 9.1 % of the analysed time. The other definitions provide LLJ detections at a very similar rate, around 2.4 %-3.1 %, thus detecting less than half as many LLJs as the ~~Rubio2022 definition~~ definition used by Rubio et al. (2022). The shear definition introduced by Hallgren et al. (2023) shows by far the ~~largest occurrence probability~~ highest detection rate with 22.6 %. For all further analysis carried out in this study, we use this definition. We choose the shear based LLJ definition for two reasons. First, its decreased sensitivity to the available range of the vertical wind profile (Hallgren et al., 2023). Secondly, the shear definition is able to capture the change of wind speed across smaller height differences, thus taking factors impacting the wind turbine performance directly into account, whereas the fall-off can also be realised across several tens or hundreds of meters.

Table 5. ~~Occurrence frequency~~ Detection rate of LLJs, as well as the absolute and relative time of detected events~~and the relative occurrence frequency~~, for all valid measurements with a total duration of 5,116.33 h.

Definition	Absolute detected time [h]	Relative amount of time [%]
~~Wagner2019~~ Wagner et al. (2019)	124.3	2.4
~~Kalverla2019~~ Kalverla et al. (2019)	146.7	2.9
~~Ranjha2013~~ Ranjha et al. (2013)	157.17	3.1
~~Rubio2022~~ Rubio et al. (2022)	467.5	9.1
~~Hallgren2023~~ Hallgren et al. (2023)	1,155.17	22.6

We analyse LLJ occurrence in dependency of several quantities, namely wind direction, time of the day and atmospheric stratification as well as the distribution of the observed core heights.

Figure 6a shows the ~~frequency of occurrence of~~ detection rate of LLJ situations in the different wind direction sectors, while Figure 6b displays the wind rose at the NG site generated from nacelle anemometer data captured at NG17, where the majority of all situations display north-westerly to south-westerly wind directions. The lowest ~~probability~~ probabilities of occurrence are present for northerly to easterly wind directions. Thus, the inflow directions we are not able to observe from ~~our~~ the lidar measurements are the least frequent ones.

For the further analysis, we separated the accessible wind direction sector into land sectors, i.e. wind directions with short fetch lengths and sea sectors, i.e. directions, where the wind travels larger distances over the sea before reaching the wind farm. The land sectors are defined from 155° to 175° and 180° to 218° (20.1% of all profiles), while the remaining directions are classified as sea sectors (79.9 % of all profiles).

We notice that the ~~occurrence frequency~~ occurrences of LLJs for land and sea sectors respectively are quite similar. LLJs are detected in 24.0 % of all recorded situations in the land sector, while they are detected in 22.2 % of the profiles for the sea sectors.

Figure 6a shows ~~,~~ that LLJs most frequently occur for southerly wind directions, especially in situations where the flow comes from the direction of the mouth of the Weser river. Here, a distinct peak is observed at the border between land and sea sectors, where the wind travels directly along the coastline for a long distance.

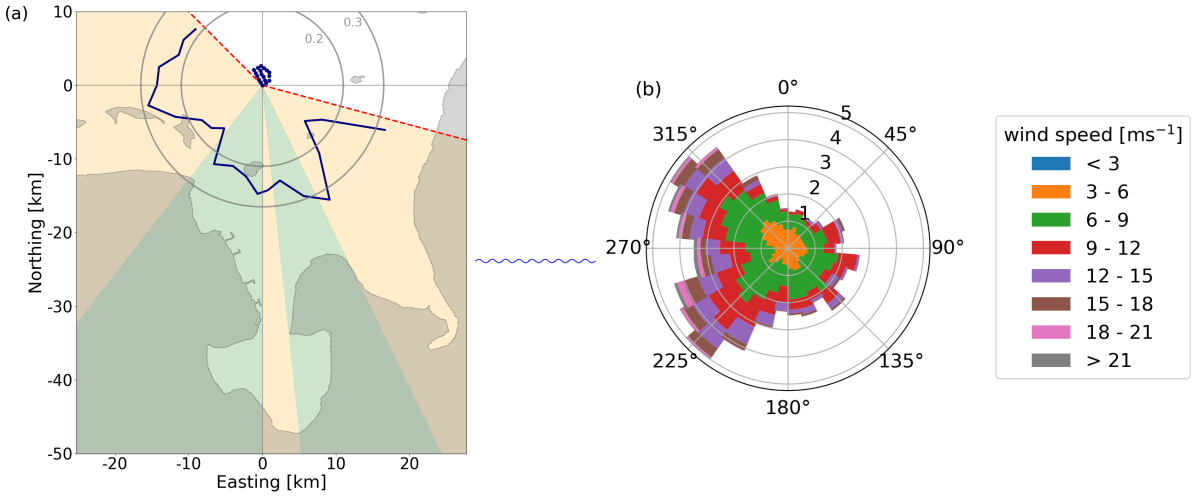

Figure 6. (a) Polar plot of the probability density of LLJ occurrences dependent on the wind direction (blue line) in the analysed wind direction sector (red dashed sector). For reference, the wind farm NG (blue markers) and coastlines (black) are shown. Further, the land and sea sectors are coloured in green and orange respectively. (b) Distribution of wind direction and corresponding wind speeds at hub height at the NG wind farm calculated from the nacelle anemometers of turbine NG17.

Figure 7 displays the diurnal cycle of LLJ occurrence at the NG wind farm for land and sea sectors. For the time of the day at which LLJs are observed, a clear pattern is present in the data. More LLJs are detected during the early morning hours, while very few are detected around noon. Although this behaviour is similar for both land and sea sectors it is more pronounced for the land sectors.

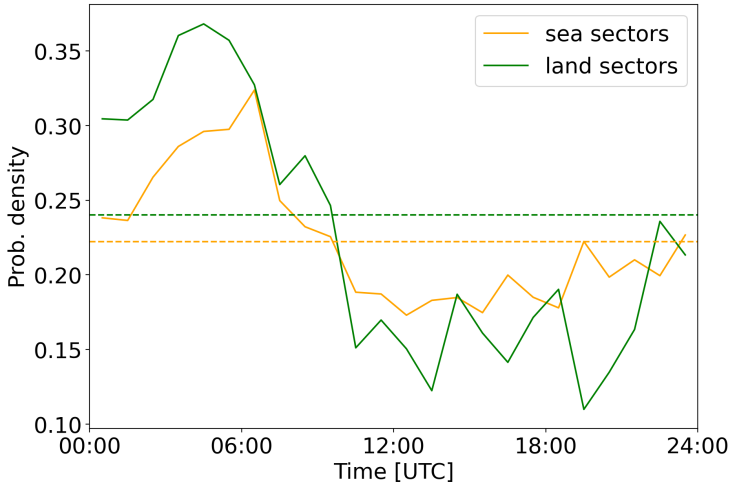

Figure 7. Daily cycle of LLJ detections for wind directions from land (green) and sea (orange) respectively (shown in Figure 6a). The dashed lines represent the mean occurrence frequency across the entire day.

Figure 8 presents the dependence of LLJ occurrence on the locally present atmospheric stratification. We use the Obukhov length as obtained from the temperature difference between the SST and the temperature at TP height (cf. Sec. 2.1) and divide our data into bins of atmospheric stability regimes (Table 6).

We observe that for the land sectors, the unstable regimes are recorded particularly frequent, while the stability regimes for the sea sector are distributed quite evenly across the measurements. Here, the major exception are very stable conditions, which are recorded only 6.61 % of the time.

Table 6. Stability regime classification based on the Obukhov length L, as proposed by Sathe et al. (2022). Further the occurrence frequency for the different stability regimes within the land sectors (20.1 % of all profiles) and sea sectors (79.9 % of all profiles) are shown.

Stability regime	L [m]	Frequency of occurrence	
		Land sectors	Sea sectors
very stable (vs)	$10 < L \leq 50$	8.3 %	6.6 %
stable (s)	$50 < L \leq 200$	15.5 %	16.8 %
near neutral / stable (nns)	$200 < L \leq 500$	5.9 %	12.0 %
neutral (n)	$\lvert L\rvert > 500$	9.3 %	17.0 %
near neutral / unstable (nnu)	$-500 \leq L < -200$	9.9 %	12.5 %
unstable (u)	$-200 \leq L < -100$	24.9 %	16.3 %
very unstable (vu)	$-100 \leq L < -50$	26.3 %	18.9 %

For the sea sectors, we observe a slight increase in frequency of LLJ occurrence towards very stable and very unstable stratification, respectively. In contrast, for the land sectors, LLJs are observed more often during extreme stratification with

an especially pronounced peak for a very stable atmosphere, where LLJs are detected for more than 50 % of all situations. However, as Table 6 shows, these very stable situations only occur quite rarely compared to other stability regimes. When comparing the land and sea sectors directly, it becomes obvious that land sectors show a higher occurrence frequency of LLJs during stable regimes, while the occurrence frequency is higher for sea sectors during unstable regimes.

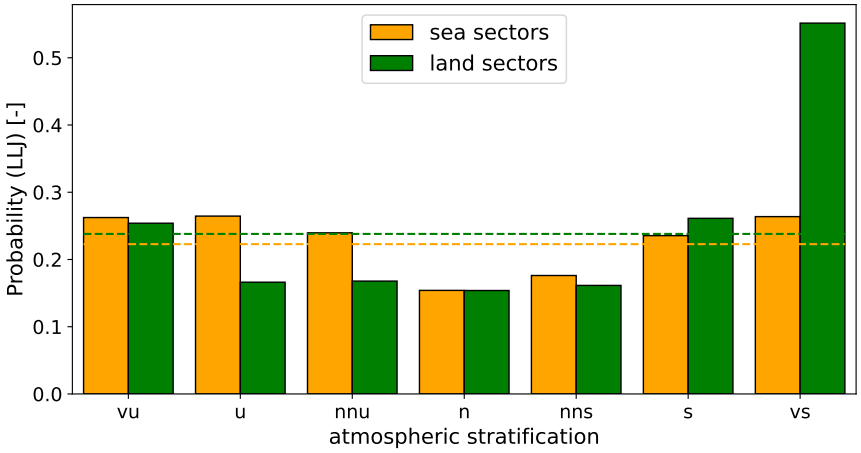

Figure 8. LLJ occurrence frequency across different stability regimes from very unstable towards very stable for land (green) and sea (orange) sectors respectively. The occurrence frequency is computed as a subset of the distribution of stratification events shown in Table 6.

Figure 9a shows the distribution of the LLJ core heights, while Figure 9b depicts the distribution of LLJ core speeds with core heights in- and outside of the rotor swept area. Further, the distribution of hub height wind speeds as recorded by the nacelle anemometer of NG17 is presented.

Regarding the height of the LLJ cores, we notice a steep increase of occurrence frequency at lower heights and throughout the rotor area. Just above the upper tip, at 165 m the maximum occurrence frequency is observed and a slight decrease of observed LLJs follows to higher altitudes. The average core height across all detected events is 188 m.

The core speeds are distributed quite unevenly across all wind speeds. For lower wind speeds a steep increase is observed, leading to a peak wind speed followed by a rather shallow decrease, resembling a Weibull distribution. We find ~~,~~that for LLJs within the rotor area ~~,~~the distribution is shifted to slightly lower values, while the distribution across all heights is very similar to the distribution of hub height wind speeds.

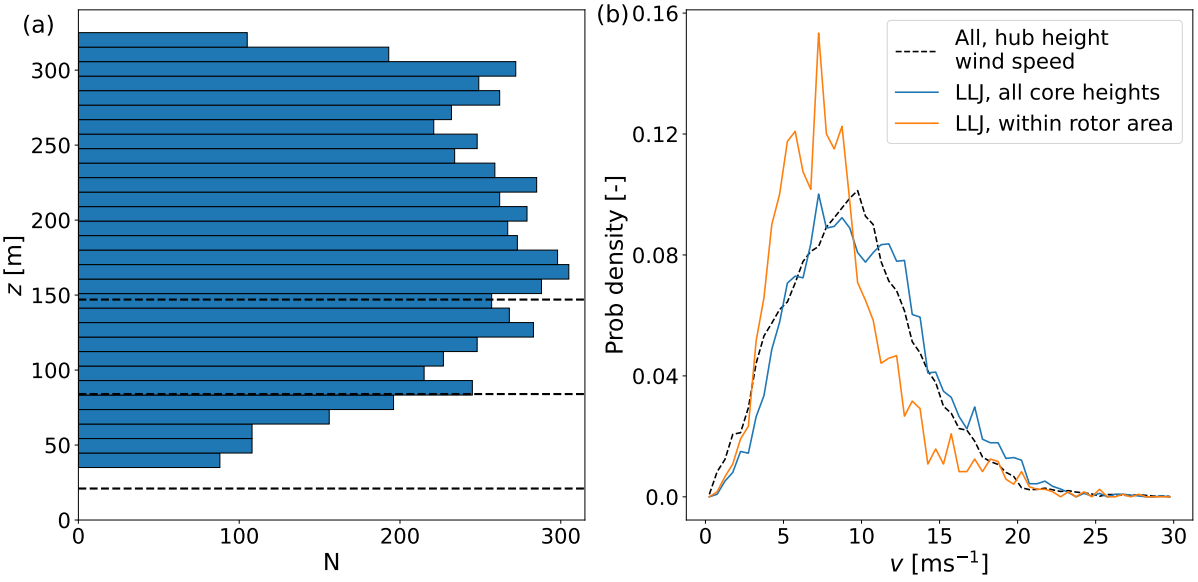

Figure 9. (a) ~~Distribution~~ Number (N) of measured LLJ ~~core~~ cores across all heights. Lower tip, upper tip and hub height are marked by dashed lines. (b) Distributions of core speeds for all observed LLJs (blue), the data subset with core heights within the rotor area (orange) together with the hub height wind speed distribution of the whole data set (black dashed line).

3.2 LLJs' influence on wind turbine energy conversion efficiency

To analyse LLJs' influence on the energy conversion process at the wind turbines, we take a look at the variability of wind speed and direction across the rotor area. To also include the effects of the different negative and positive shears and veers within the profile, we analyse the average of the absolute differences of wind speed and direction across the rotor swept area:

$$\overline{|\Delta v|} = \frac{\sum_i |v(z_{i+1}) - v(z_i)|}{D} \quad \text{and} \quad \overline{|\Delta \Theta|} = \frac{\sum_i |\Theta(z_{i+1}) - \Theta(z_i)|}{D}; \quad \text{where}: z_{\text{low}} \leq z_i \leq z_{\text{up}} \tag{16}$$

with the upper and lower tip height z_{up} and z_{low} respectively and the rotor diameter $D = 126\,\text{m}$.

Figure 10 shows the average veer (a) and shear (b) across the rotor area for profiles with and without LLJs respectively. Here, we notice a skew of the LLJ profiles towards higher veer and shear values. This is also represented in the mean values of wind shear and veer which are both observed to be larger during LLJ events (cf. Table 7).

Table 7. Average wind shear and veer for LLJ and non-LLJ situations respectively.

	$\overline{\lvert\Delta v\rvert}$ [s^{-1}]	$\overline{\lvert\Delta\Theta\rvert}$ [° m^{-1}]
non-LLJ	0.019	0.189
LLJ	0.037	0.318

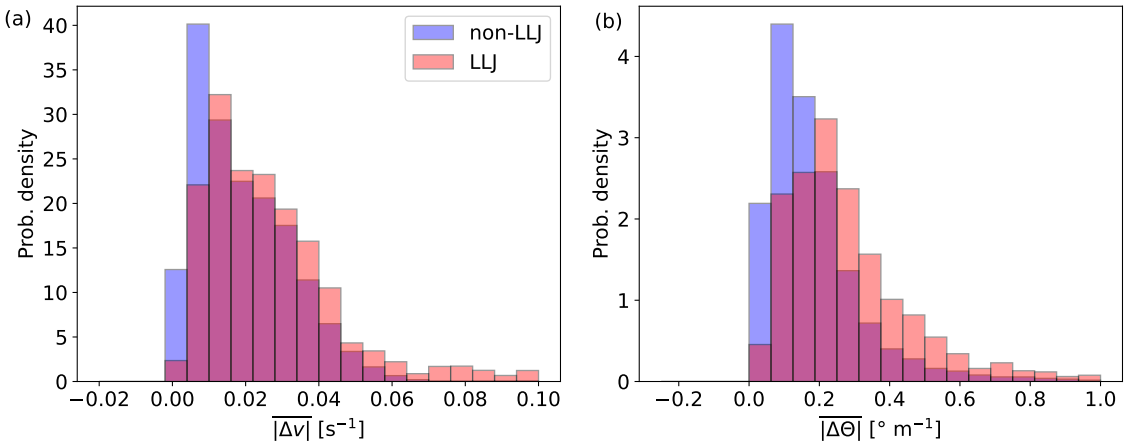

Figure 10. (a) Average wind shear and (b) veer across the rotor swept area for all measured profiles not containing LLJs shaded in blue and those containing LLJs in red.

Figure 11a shows the averaged apparent power production within the respective wind speed bins during free inflow situations (cf. Sec. 2.4). While the apparent power production is lower during LLJ events throughout all REWS bins, we observe larger differences between the two in the upper partial load range. As the number of detected events decreases towards higher wind speeds, the uncertainty associated with these wind speed bins is observed to increase as well. A maximum difference between
405 LLJ and non-LLJ cases of 8.9 % of the rated power is observed at 13 ms^{-1}.

Our analysis also shows that most LLJs within the rotor area are observed at REWS in the middle of the partial load range, with a maximum at around 7 ms^{-1} (Fig. 11b).

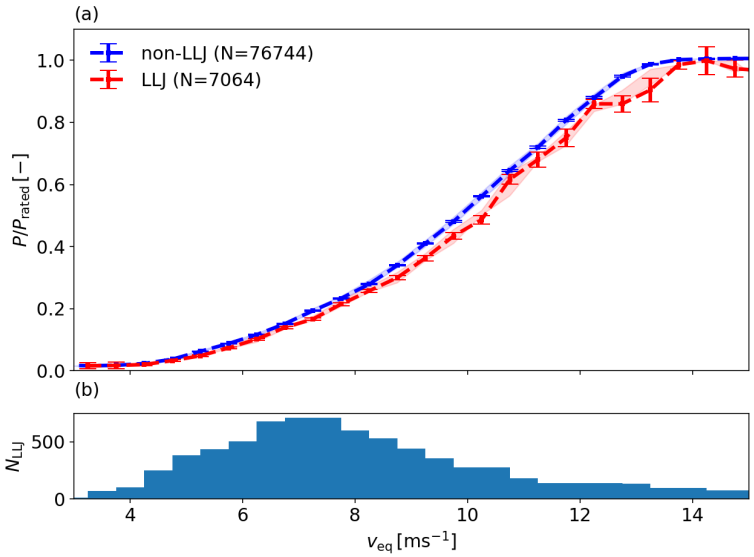

Figure 11. (a) Average apparent power production per binned v_{eq} (cf. Eq. 11) during non-LLJ situations (blue) and LLJ situations (red). Error bars depict the standard error of the mean of the apparent power within each wind speed bin. Shaded areas depict the corresponding uncertainty intervals obtained by computing power curves with added and subtracted uncertainty estimations respectively (cf. Section 2.4). (b) Number of LLJs per wind speed bin.

3.3 Analysis of the fluctuations in power production

To investigate the fluctuation of the power production during LLJ situations, we calculate its fluctuation $\mathrm{PO}_{\mathrm{TI}}$ according to Eq. 6. Moreover, to make the results more representative we separate the data based on the present stability regime.

Figure 12 shows box plots and the median of the $\mathrm{PO}_{\mathrm{TI}}$ per 10-minute interval over the prevailing stability regime. Here, we observe that the fluctuations in apparent power production are higher for LLJ situations across almost all the different stability regimes, except for near-neutral unstable (nnu) and unstable (u) conditions. We observe a general trend towards higher $\mathrm{PO}_{\mathrm{TI}}$ for increasingly unstable stratification for non-LLJ situations, while we observe similar median $\mathrm{PO}_{\mathrm{TI}}$ during stable and (very) unstable situations with LLJs present. We also observe a slight increase of the median $\mathrm{PO}_{\mathrm{TI}}$ for non-LLJ situations from neutral towards very stable stratification.

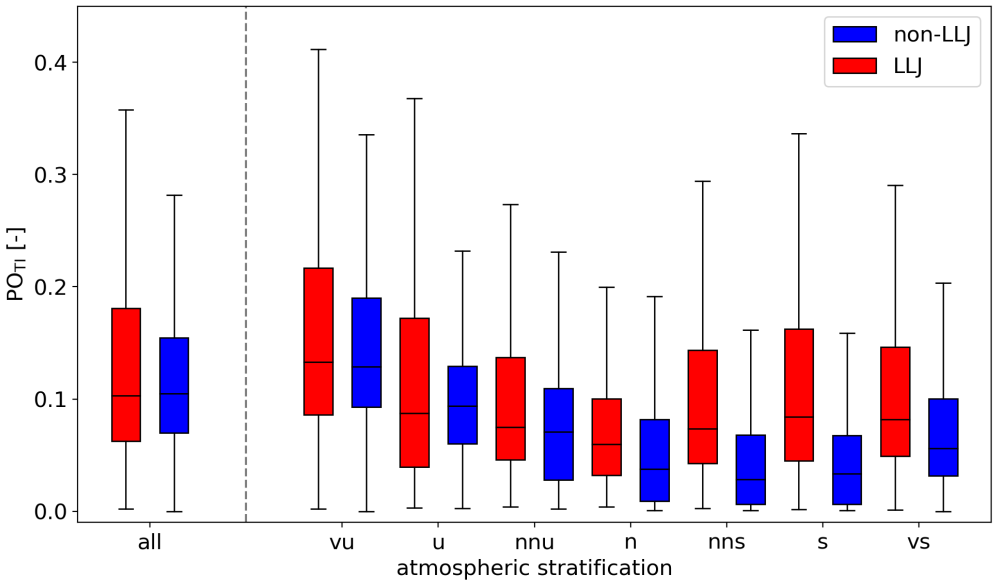

Figure 12. Box plots of the normalised standard deviation of the power production $\mathrm{PO_{TI}}$ for LLJ and non-LLJ situations, respectively, across all the different stability regimes. The boxes are limited by the first (Q1) and third quartile (Q3) respectively, with the whiskers representing $Q_1 - 1.5\,IQR$ and $Q_3 + 1.5\,IQR$, with IQR the interquartile range. The horizontal black lines represent the median $\mathrm{PO_{TI}}$.

3.4 Aeroelastic simulation of wind turbine performance

To further deepen our understanding of how LLJs affect wind turbine performance, we analyse the results of 156 aeroelastic simulations, each with a different type of vertical wind speed profile, but the same veer-corrected REWS of the NREL 5MW offshore reference turbine (cf. Sec. 2.5).

Table 8 lists the average power production and $\mathrm{PO_{TI}}$ during the aeroelastic simulation of the turbine response to the generated inflow profiles. When analysing the average power production across all simulations, we observe a slightly increased power for the uniform inflow profiles. The average power production between LLJ and logarithmic profiles, however, is very similar. Concerning the $\mathrm{PO_{TI}}$, our simulations show the highest power fluctuation for LLJ profiles, while it decreases for logarithmic profiles and is lowest for the uniform inflow profiles.

Table 8. Average power production and $\mathrm{PO_{TI}}$ across all simulations for the different types of profiles. Further, the number of simulations for each profile type is displayed.

	uniform	logarithmic	LLJ
$\overline{P}$ [kW]	1642	1619	1619
$\mathrm{PO_{TI}}$ [-]	~~0.0091~~ 0.009	~~0.0101~~ 0.010	~~0.1112~~ 0.011
N	12	36	108

One important factor, assumed to have a major influence on the observed power production is the absolute shear of the wind speed across the rotor area. Within our simulations, we observe a similar result.

Figure 13a shows the relation between the absolute shear in the ~~profile~~ profiles and the temporally averaged power production of the turbine for each of the simulated inflow ~~profile~~profiles. Here, we observe that with increasing shear the generated power decreases. Further, we also observe ~~,~~ that this relation is quite linear for logarithmic wind profiles, whereas a more spread picture is seen for the LLJ profiles. ~~Here, the~~ The minimum power production is not observed at the highest average shear of $0.064\,\mathrm{s}^{-1}$ across the rotor area, but already at $0.035\,\mathrm{s}^{-1}$.

A similar effect is observed concerning the veer across the rotor area (Fig. 13~~a~~b). Again, ~~a strong relation between increasing shear and decreased~~ power production is ~~found in the data~~seen to decrease strongly with increasing veer. In contrast to the shear analysis, the decrease in observed power production for LLJ profiles seems to follow a linear trend.

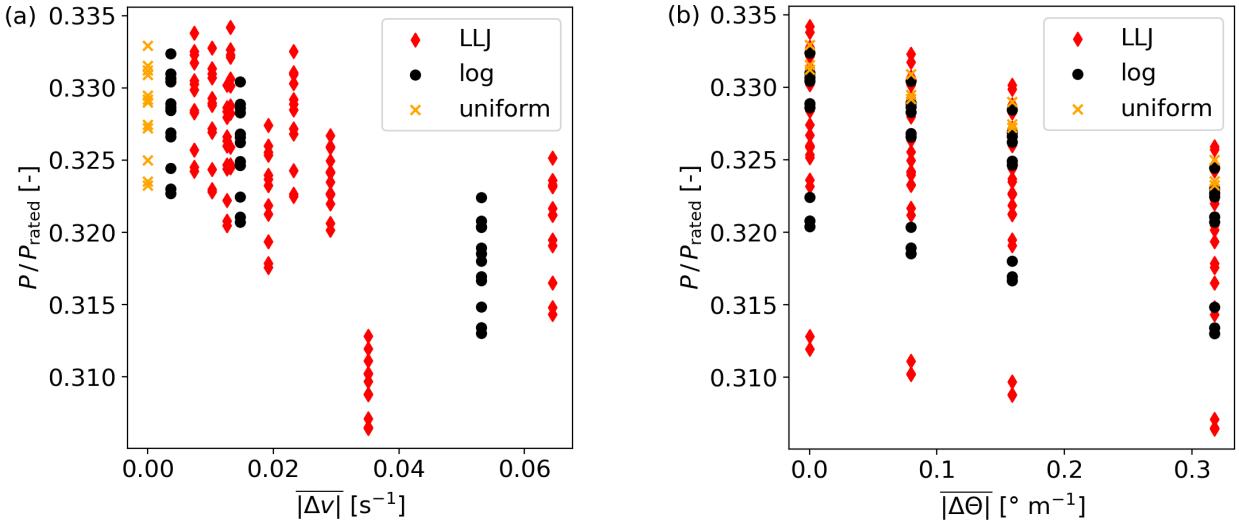

Figure 13. Simulated normalised power production over the shear (a) and veer (b) of the wind profiles across the rotor swept area for each of the simulated inflow profiles. Uniform wind profiles are depicted as orange crosses, logarithmic profiles as black circles and the LLJ profiles as red diamonds.

Next, we also analyse the relation between ~~TI~~ turbulence intensity (TI) and average power production. Here, only a very small difference between the different simulated TIs is observed. From the data, we see a slight increase in power production with increasing TI. However, as Figure 14 shows, the fluctuations within the three TI regimes are quite high and only a slight increase in the median power is seen.

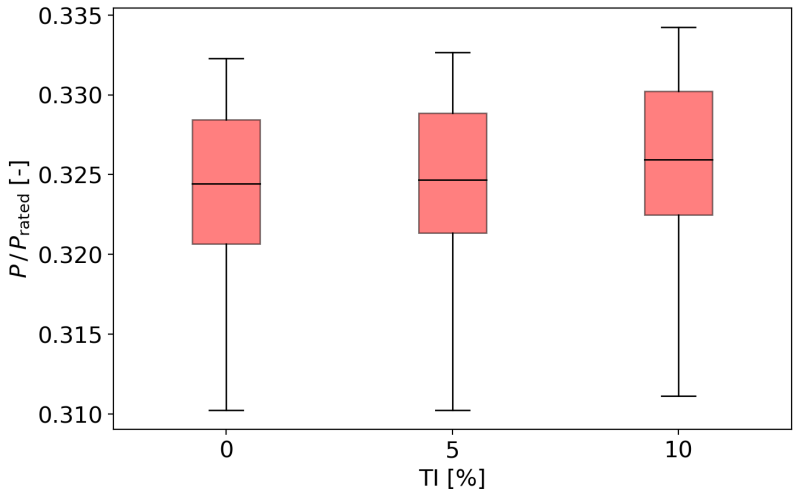

Figure 14. Boxplot of the power production for all simulated profiles with respect to the chosen TI. The black lines represent the median for each regime, while the box edges show the limits of the first and third quartile of the data.

In the following, we want to highlight the different characteristics of LLJ profiles, i.e. fall-off, width and core height and how they influence the power production of the turbines.

Figure 15a shows the average power production over the magnitude of the fall-off and the height of the LLJ core. We notice a decreasing trend for the power with increasing fall-off of the LLJ profiles. Also, we see lower power production for LLJs with their core height at the upper tip of the turbine. The opposite trend is observed for the LLJ core width ε (Fig. 15b). Here, an increase of power is observed for wider LLJ cores. Also, the distribution of power production is far broader for very narrow LLJ cores compared to larger ε.

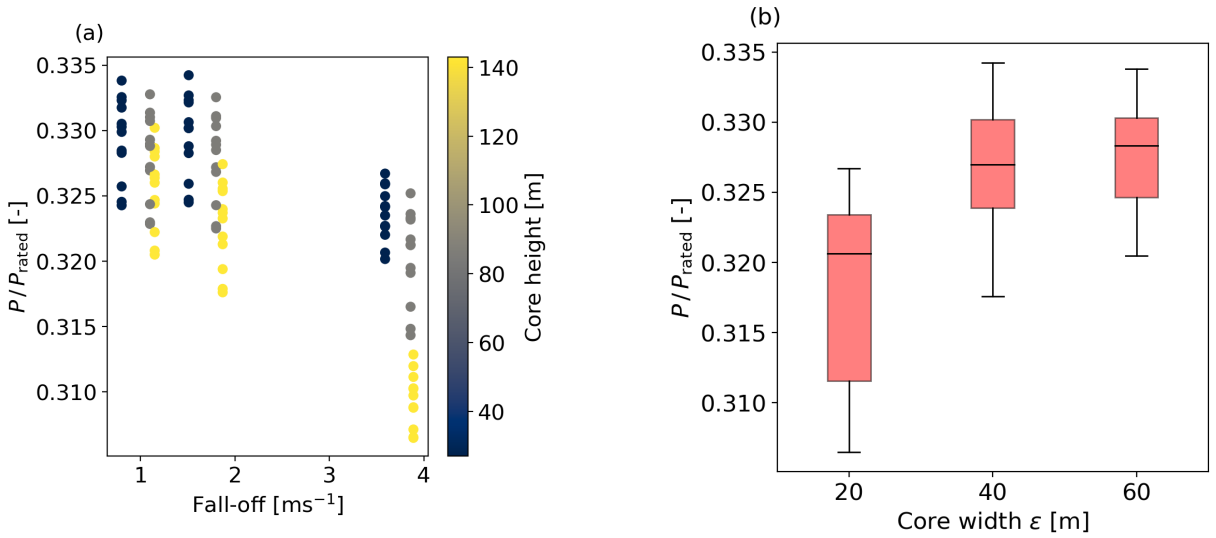

Figure 15. Average power production during simulations with LLJ wind profiles plotted over the fall-off and the core height as colour code (a) and the width of the LLJ core in (b) where the box represents the limits from first and third quartile and the black line the median value.

4 Discussion

In the following, we discuss uncertainties within the lidar measurements and their processing, the applied LLJ definitions and the occurrence statistics of the LLJs at the observed location, as well as their impact on the power conversion efficiency of the turbines.

~~Analysing LLJs in an~~ Our LLJ analysis in the offshore environment relies on the lidar sensing of vertical wind profiles and thus ~~the~~ several sources of uncertainty have to be considered. ~~Previous studies relied on the measurement~~ To account for the pointing accuracy of the lidar, we consider the earth's curvature and the tilt and roll of the lidar. Moreover, uncertainties such as measurement uncertainties of the wind speed and direction caused by the lidar, have been included in the analysis using the Gaussian uncertainty propagation presented in App. B. Applying all the different algorithms of data correction in post-processing, allows for a precise classification of all measured data points in the correct height bands when generating vertical wind profiles.

Previous studies, applying remote sensing methodologies to estimate vertical wind profiles, typically relied on measurements using the Doppler-beam-swing (DBS) ~~and~~ or velocity-azimuth display (VAD) methods. ~~The commonly used DBS technique retrieves~~ Both VAD and DBS scans retrieve a wind profile above the lidar in a comparably small measurement volume. As we performed multiple PPI scans at different elevations ~~,~~ our measurements encompassed a larger ~~area with considerable variability in the wind field. However, generating the wind profiles from the volumetric 3D wind field, our results at hub height showed a good agreement with the wind speed obtained from the operational data of the turbine NG17. The correlation coefficient between the two variables lies at R^2=0.97. Further, we also compared~~ volume then VAD or DBS scans, several factors, such

as the spatial development of the vertical wind profile when approaching the wind farm and local inhomogeneities must be considered.

Regarding the development of wind speeds when crossing from land to sea, Goit et al. (2020) and Barekzai et al. (2025a), both suggested an increase of wind speed with increasing distance to the shore. Goit et al. (2020) present, that the development of an internal boundary layer caused by the crossing of the wind from on- to offshore regions is observed within their lidar scans. Here, the authors observe no further development within their measurement volume after 2 km off the shoreline. Barekzai et al. (2025a) observe from mesoscale simulations, that while wind speeds still increase at distances of 250 km offshore, their differences within a 10 km range about 15 km off the shore are in the range of approx. 0.8 ms^{-1} 10 m above the sea surface and only in the range of approx 0.15 ms^{-1} at higher altitudes.

With respect to the local inhomogeneities in the flow, Goit et al. (2020) also performed horizontal PPI scans with an elevation of 13.2° and an azimuth opening of 40° encompassing larger measurement volumes compared to VAD or DBS scans in a near-coastal location in Japan. They showed that derived wind speeds and wind directions from elevated PPI scans were in good accordance with nacelle wind speed and direction measurements as well as with wind profiles derived from DBS lidar scans.

Since we aim at analysing larger scale structures, i.e. LLJs persisting over the scale of the wind farm and at least 10 minutes, a possible spatial and temporal averaging of small fluctuations due to our measurement and analysis strategy is seen more supportive for our goals than hindering.

To reinforce this claim, we compare vertical wind profiles retrieved using our volumetric approach to more ~~localized~~ localised wind profiles obtained via a method similar to Visich and Conan (2025) for ~~one month of data. Here, we observe average absolute differences between the two methods below 1 across almost all heights~~ the entire time frame as well as wind speed and direction measurements from the turbine NG17. The profiles we retrieve from the volumetric approach are generally in good accordance with the more localised wind profiles across all heights and multiple wind directions. However, we observe that the availability and quality of profiles decreases dramatically when limiting the used data points to generate profiles. The fluctuation of the wind shear also increases with these localised profiles leading to an increase in algorithm detected LLJ events. We mainly attribute this to the fact, that due to the wide azimuth sector as well as the 16 successive scans with increasing elevations, the local data availability per 10-minute interval is decreased in the smaller volumes, leading to a decreased quality in retrieved profiles. The LLJs detected from localised profiles are often not persistent LLJ phenomena, but rather artifacts resulting from strongly fluctuating wind speeds with height due to an insufficient number of samples per measurement height in each averaging interval of 10 minutes. ~~The LLJ detection rate for the two different methods increases from 33.1 using the volumetric approach to 36.6 using the metmast approach, despite a considerably lower data availability of the metmast style profiles, dropping from 99.5 obtained from the volumetric approach to 79.9 .~~ This establishes the multi-elevation lidar ~~measurements~~ PPI scans as a valuable ~~asset~~ technique for the wind profile generation. ~~Further, we accounted for several uncertainties like the earth's curvature and the tilt and roll of the lidar in post-processing, increasing the pointing accuracy of the positions of our measurements. Further uncertainties, such as measurement uncertainties of the wind speed and~~

direction caused by the lidar, have been included in the analysis using the Gaussian uncertainty propagation. While the method applied in this study is not used often, it provides valuable results and proves to be well suited for this specific application.

A more elaborate comparison of the two approaches, as well a comparison against nacelle measurements from NG17 is presented in Appendix C.

In the literature several different LLJ definitions are used, all coming with individual benefits and drawbacks. Within our work, we present the characterisation of the occurrence of LLJs and their properties. Further, to To analyse wind turbine power under the influence of atmospheric LLJs we use long-range lidar and SCADA data from the wind farm Nordergründe. For our analysis, we We mainly use the definition of an LLJ proposed by Hallgren et al. (2023). The main characteristic of this definition is that instead of using the absolute and/or relative fall-off of the wind speed it makes use of the shear of the wind speed. Hallgren et al. (2023) show that this makes the provided definition less sensitive to limited measurement heights as typically achieved with met masts or standard lidar profilers. This is especially important in our case, as we generated wind profiles from multi-elevation PPI scans, reaching maximum heights of around 350 m, what is comparable to measurement heights of a lidar profiler. Other studies using e.g. reanalysis data make use of increased measurement heights, thus also showing occurrences of LLJs at higher altitudes (e.g. Kalverla et al., 2019). Also, the shear-based definition is more applicable to wind energy-related purposes, as it concentrates directly on the shear, a property which is shown to have a non-negligible influence on the conversion efficiency of a wind turbine (Dörenkämper et al., 2014; Murphy et al., 2020). Using this local property instead of a fall-off -- which can in theory be realised over a large height difference -- also allows a precise description of the inflow conditions across the rotor area. Further, we also observe large discrepancies between the shear definition and the fall-off-based definitions concerning the detected LLJ events, with the shear-based definition detecting ten times more LLJ events than the most restrictive criteria and double the amount compared to the least restrictive definition (cf. Table 5).

Our results show that LLJ occurrence frequency is detection rates are highly dependent on many factors, as large differences emerge compared to other studies (e.g. Rausch et al., 2022; Baas et al., 2009), thus showing a strong dependence of LLJ occurrence on the measurement site, the applied measurement techniques and the measurement period. Next to the environmental conditions, our results also show a very strong difference based on the different LLJ definitions present in the literature (cf. Table 5). The difference in occurrence frequency for varying locations is further backed up by mesoscale simulations which found a relation between distance to the coast and LLJ occurrence frequency (?)(Barekzai et al., 2025b). Also, as we are only able to observe a limited wind direction sector, LLJs from a north-easterly direction, i.e. fetch direction from the open sea, are not captured in this study. Also, the proximity of the measurement location to the Wadden Sea makes it a complex site, as this way, the sea surface temperature and thus the prevailing atmospheric stratification are strongly dependent on the current tide (Appendix A). Regarding the influence of the atmospheric stratification on the detection rate of LLJs, we observe a similar behaviour for both land and sea sectors as the occurrence frequencies increase towards both stable and unstable stratification. While for unstable stratification they occur more frequently from sea sectors, LLJs show higher probabilities for stable stratifications when emerging from coastal directions. Our results also show that the amount of detected LLJ cores increases with height, up to a local maximum at 165 m. In our study, we observe an increased occurrence frequency during unstable

conditions, compared to previous studies (e.g. Wagner et al., 2019). Based ~~in~~ on the directional analysis of the occurrences, we assume these to be features advected from the land masses. Further, as we ~~are only able to~~ measure temperature differences between the TP of the turbine and the sea surface, ~~the stability estimate allows us to draw conclusions about this region.~~ we bin our data based on the near-surface stability estimate, retrieved from the measurements.

For increased altitudes, the number of detected core heights seems to stagnate and even decrease. However, at these altitudes also the availability of measurements decreases notably, i.e. less wind profiles are available for LLJ detection. Further, within our measurements, we are only able to observe wind speeds up to heights of 350 m. Hallgren et al. (2023) show that extending this height up to 500 m leads to a significant increase of identified LLJs. For some of the observed LLJ occurrence characteristics, such as e.g. the diurnal cycle, similarities to the literature are observed (e.g. Rausch et al., 2022), independent of the location and the distance to the mainland.

As the main finding, we observe a less efficient power conversion efficiency of turbines in LLJ situations compared to non-LLJ situations, with a maximum difference of 8.9 %. As this difference is observed directly below rated wind speed, it must be treated carefully. One driver for this decreased efficiency is the increased shear across the rotor area which is shown to be detrimental to the performance of wind turbines (Dörenkämper et al., 2014). This trend is further verified by aeroelastic simulations carried out within our study. The results show that not necessarily the anomaly in the shape of the profile leads to a reduced apparent power production, but rather the increased absolute shear. This is also seen from the simulations with different shapes of LLJ profiles, where a lower production is observed for situations with higher absolute shear. Also, an increased veer across the rotor area is observed for LLJ profiles at NG, which according to the results of the aeroelastic simulations further decreases turbine efficiency, even when comparing situations with the same wind veer-corrected REWS. Moreover, Mortarini et al. (2018) observed a lower turbulence intensity below the LLJ core. This has a slightly negative effect on a wind turbine's power production (Dörenkämper et al., 2014). The trend we observe is further backed up by Zhang et al. (2019), who also showed a decreased power production for LLJ-situations with the same hub height wind speed as for a logarithmic wind profile within their simulations, despite using rather weakly pronounced LLJs in their study. Here, Zhang et al. (2019) also found that this deficit is highly dependent on the relative position of the wind speed maximum inside the rotor area, which is confirmed by our simulations. While the average apparent power decreased during LLJ events, we observed an increase in the fluctuation of the production, especially during stable stratification. One factor impacting this behaviour can be the rise of intermittent bursting of turbulence, which can be triggered by LLJs (Ohya et al., 2008) and may have an effect on the performance of the turbines.

While in our study, we found decreased power conversion efficiency during LLJ situations, Gadde and Stevens (2021) found increased power production during LLJ-situations in a numerical study. However, their Large-Eddy Simulations compare wind profiles with different REWS, by deriving their wind profiles from varied meteorological parameters. As a result, LLJ situations show a higher availability of energy in the wind and thus the power production is increased. This further emphasises the use of a different metric - like the REWS - to compare power conversion efficiency for different wind profile shapes. We ~~tried to evaluate~~ aim at evaluating the performance of turbines with similar energy availability and thus aimed to compare situations

with similar REWS. This way we can show how the energy conversion process becomes less efficient during LLJ events, with the main drivers here being the increased shear and veer across the rotor area.

Despite the observed efficiency decrease during LLJ situations, we cannot draw any indication on whether the effect on the annual energy production (AEP) is negative or positive due to several reasons. First, frequent LLJ situations affect the wind speed distribution at hub height in addition to their effect on wind shear and REWS. Secondly, LLJ occurrence is correlated with atmospheric stratification and turbulence characteristics, both impacting the wind turbine wake development and AEP (St. Martin et al., 2016; Cañadillas et al., 2022). Finally, the influence of LLJs on wind farm wake losses is an open question. Nonetheless, our results suggest that the consideration of LLJs in the AEP calculation at sites with high occurrence frequencies of such situations could result in reduced uncertainties in predicted energy production in the future.

5 Conclusion

In this study, we investigate the influence of atmospheric low-level jets (LLJ) on offshore wind turbine power conversion efficiency based on scanning lidar measurements, wind farm operational data at the Nordergründe wind farm and aeroelastic simulations. We observe LLJs based on our volumetric wind profiles between 2.4% and 22.6% of the investigated time for undisturbed inflow towards the wind farm from wind directions between 100° and 320° depending on the used definition~~, thus proving~~ . This proves them to be a relevant phenomenon to be considered for wind power applications. Most LLJs observed at this location have core heights above the rotor-swept area. Thus, their importance for wind energy-related processes will increase in the future with larger turbines being installed. When compared to other studies, it becomes clear that the LLJ occurrence frequency is dependent on the observed location as well as the observed time frame and meteorological conditions, e.g. atmospheric stratification, wind direction and fetch. Concerning the location several factors can play a role, e.g. the distance to the coast, predominant wind directions and other special features such as the proximity to the Wadden Sea, which has a large influence on the sea surface temperature, which in turn impacts the atmospheric stratification.

Previous studies relied on the hub height wind speed to compare different types of wind profiles and their influence on the energy conversion process in wind turbines. Instead, we explicitly use the wind-veer-corrected rotor equivalent wind speed (REWS) as our reference wind speed, thus following the guidelines provided by IEC 61400-12-1 (IEC, 2017). This formulation ~~,~~ compared to just the hub height wind speed ~~,~~ incorporates the change of wind speed and direction across the rotor and thus is a more suitable measure for the energy flux through the rotor area. Applying REWS as a reference, our study showed that wind turbines are not able to harvest the energy contained in the wind to the same extent during LLJs, as they can do during non-LLJ situations. Thus, we propose an incorporation of LLJs into the AEP calculations in strongly affected regions to possibly reduce uncertainties in the energy prediction. For the variability of the power production, we observe higher fluctuations during LLJ situations throughout various stability regimes, with stronger differences emerging especially during stable stratification.

Although a clear trend is observed for the considered performance parameters, i.e. the power production and its fluctuation from field measurements and aeroelastic simulations, more extensive research on larger datasets is required to further develop our understanding of the interactions between wind turbines and LLJs. This includes the wake recovery inside wind farms

during LLJ situations as well as their possible impact on wind turbine loads due to the uneven distribution of the wind speed and especially direction over the rotor area.

Future studies on LLJ interaction with wind turbines and wind farms would benefit from adapted lidar inflow measurements reaching up to higher altitudes and additional local wind profiles measured in front of the farm. This would allow for an improved LLJ detection even above upper blade tip height as well as the possibility to compare volumetric wind profiles to measured local profiles. Further, the development of vertical wind profiles and LLJs with increasing distance from the shore could be studied. Additional load measurements on wind turbines would allow to study the influence of LLJs on wind turbine loading.

Data availability. Wind farm operational data from Nordergründe are confidential and not published. Lidar and meteorological data are not published. Recent values of water level, water temperature and further quantities measured at the lighthouse Alte Weser are available at https://www.pegelonline.wsv.de, access to historical data is limited (WSV, 2023). The OSTIA dataset is publicly available via https://doi.org/10.48670/moi-00165 (Good et al., 2020).

Appendix A: Atmospheric stability and sea surface temperature

The main quantity to describe the static atmospheric stratification in the marine boundary layer is the difference between the air temperature at a given height and the sea surface temperature (SST). While the air temperature can be measured with manageable efforts, knowledge about the SST is harder to achieve. Using a measurement buoy is expensive and prone to damage. Previous studies used a buoy in a far offshore location to measure SST (e.g. Schneemann et al., 2020). In periods without the buoy measurement, the SST from the OSTIA data set providing one value per day (Good et al., 2020) proved useful. For the present study in a near coastal area with mud flats (Wadden Sea) and a large effect of tidal currents, we expect faster changes in the SST than being resolvable with OSTIA. Therefore we used a combination of two infrared sensors (Heitronics CT09 and CT15 with internal correction for sky radiance) installed on the transition piece of the wind turbine NG17.

Combining our SST measurements at NG17 with water level measurements from the Alte Weser lighthouse (AW), located roughly 5.2 km from the wind farm, we observe a clear dependency between the sea level and a change in the SST. At times of high tide, the SST decreases by up to 3 °C compared to low tide. Figure A1a shows the water level at the lighthouse Alte Weser with level maxima detected and marked for one exemplary period of eleven days. Figure A1b depicts the SST measured with the IR sensors at the wind turbine NG17. This suggests that cooler water is transported by the rising tide towards the measurement location, while the opposite takes place at low tide.

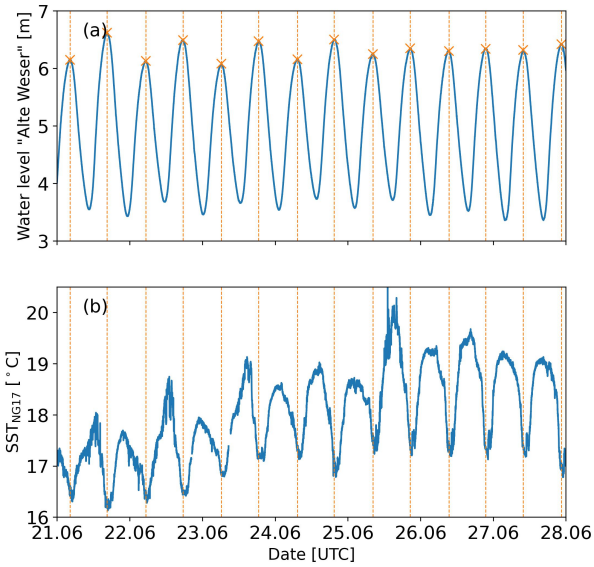

Figure A1. (a) Water level measured at the lighthouse Alte Weser (WSV, 2023). Maxima are detected with a peakfinder and marked ($\times$). (b) Sea surface temperature measured at the wind turbine NG17 in the offshore wind farm Nordergründe with approx. 5.2 km distance to Alte Weser. Times of high tide detected in (a) are marked by vertical dashed lines.

Figure A2 compares three different sources of the local water temperature. Aside from our IR-SST measurements at the turbine NG17 $\mathrm{SST}_{\mathrm{NG17}}$ we show two publicly available data sources, namely the water temperature measured at the lighthouse Alte Weser $T_{\mathrm{AlteWeser}}$ (WSV, 2023) and the SST from the OSTIA data set $\mathrm{SST}_{\mathrm{OSTIA}}$ (Good et al., 2020). The water temperature at Alte Weser is measured using a sensor WTW TetraCon 700 IQ SW. It is installed at the foundation of the lighthouse in north-westerly direction in a fixed position of approx. 1 m below mean tidal low water.

The OSTIA data set provides one SST value per day. Here we chose the values from the closest offshore grid point to the NG wind farm.

Both $\mathrm{SST}_{\mathrm{NG17}}$ and $T_{\mathrm{AlteWeser}}$ show a periodic temperature fluctuation with the tidal currents that can not be resolved by $\mathrm{SST}_{\mathrm{OSTIA}}$. Concerning the correlation between the different temperature measurements, we observe good agreement.

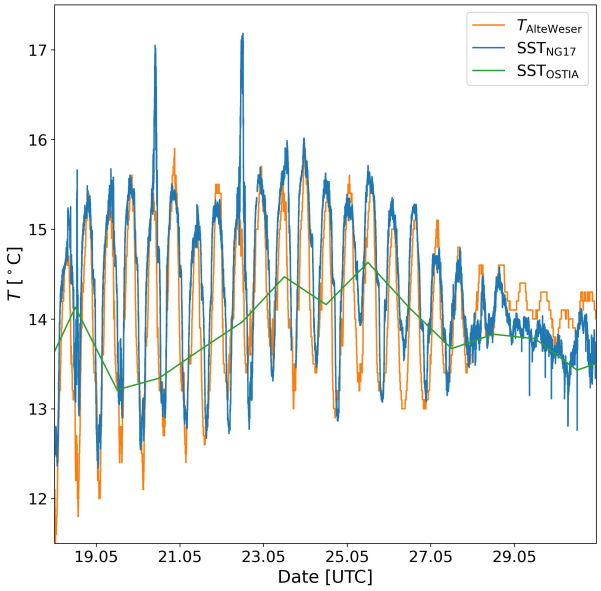

Figure A2. Water temperature at the lighthouse Alte Weser $T_{\mathrm{AlteWeser}}$ with a resolution of 1/60 Hz (WSV, 2023) (orange), sea surface temperature $\mathrm{SST}_{\mathrm{NG17}}$ measured with an infrared sensor from the transition piece of turbine NG17 in the offshore wind farm Nordergründe resampled to one minute (blue), and sea surface temperature from the OSTIA data set $\mathrm{SST}_{\mathrm{OSTIA}}$ (Good et al., 2020) at a grid point in the western vicinity of Nordergründe with one value per day (green).

Figure A3 shows the annual fluctuation of the SST as captured by the different data sources. Here, we average the data from the Alte Weser lighthouse and the local SST measurements at NG to daily values. The comparison shows that all three methods capture the daily fluctuations and the annual trend quite well.

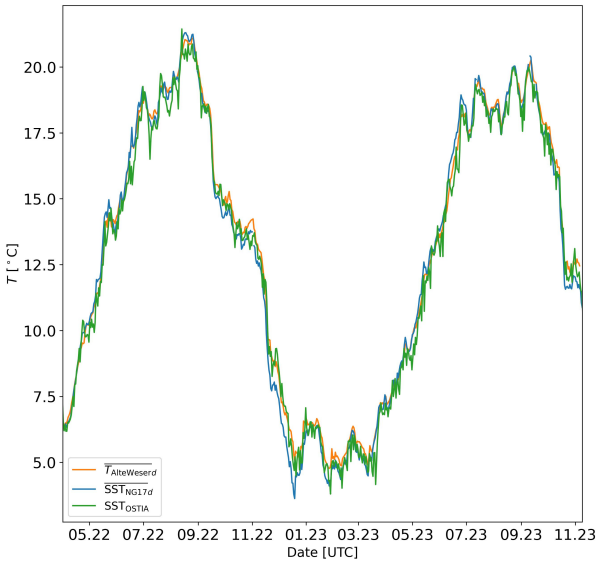

Figure A3. Water temperatures from Alte Weser, NG17 and OSTIA as in Figure A2 but data from Alte Weser and NG17 resampled to daily values. More than one year of data is shown.

To provide a more statistically sound analysis, we performed orthogonal distance regressions (ODR) between the one minute averages of AW and NG as well as the OSTIA data and the daily average of the NG measurements. Figure A4 shows scatter plots of the SST measurements from different data sources, with Fig. A4a presenting the correlation between the high-resolution data at AW and NG and Fig. A4b displaying the correlation between NG and OSTIA. For both different combinations we observe a very high Spearman correlation coefficient of $R^2 > 0.99$. Further, we also observe a slope very close to one and small positive offsets for AW and OSTIA compared to the NG data.

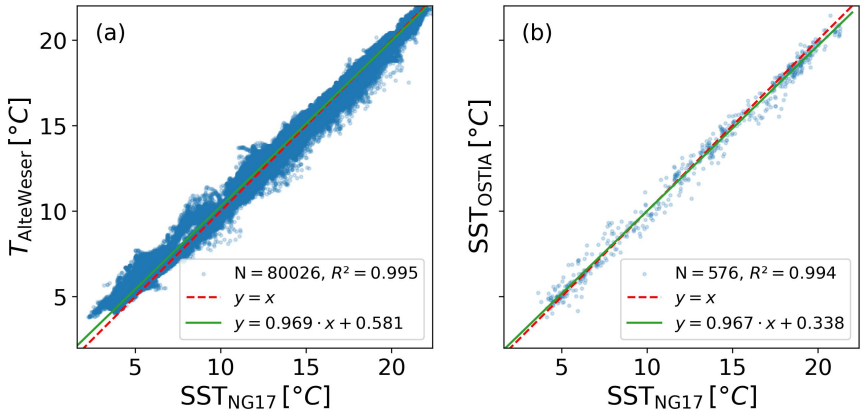

Figure A4. Scatter plots showing the correlation between the SST measurements at NG17 and water temperature measurement at the lighthouse Alte Weser (a) and the OSTIA data set (b), respectively. The $y = x$ curve is depicted as a dashed red line and the regression line in green.

Finally, we compare the stability estimates obtained from the three different temperature measurements. Here, we use the dimensionless $\zeta = z_{\mathrm{TP}} \,/\, L$-parameter as no discontinuity around the zero crossing is present.

Figure A5 shows the correlations between the different stability estimates. Both combinations show a Spearman correlation coefficient of $R^2 > 0.88$ and thus provide a quite good correlation. However, there is a visible difference between high-resolution data and the OSTIA data set. The correlation coefficient between AW and NG is considerably higher at $R^2 = 0.961$, compared to the correlation of the high-resolution data with OSTIA-based stability estimates at $R^2 = 0.882$. For both datasets, we perform an ODR and observe regression lines with almost negligible bias and a slope close to one.

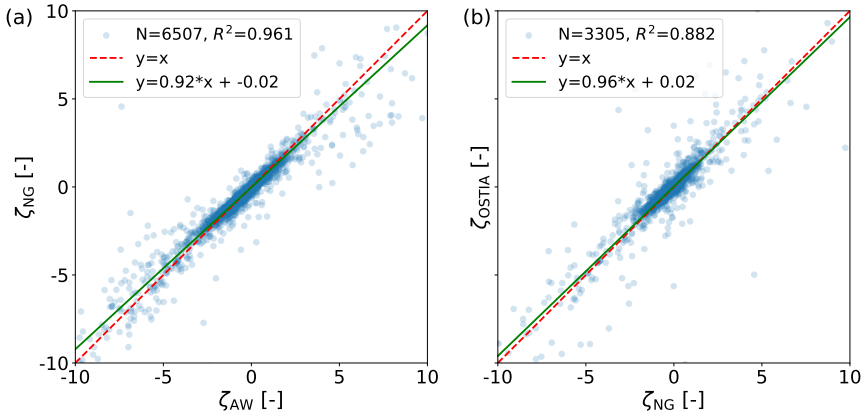

Figure A5. Scatter plots of the ζ-parameters derived from all three different temperature measurements. In (a) the correlation between Alte Weser and NG is shown, while (b) shows the correlation between between NG and OSTIA. A regression line determined via ODR is drawn in green with the regression parameters shown in the legend. The $y = x$ curve is depicted as a dashed red line.

Appendix B: Estimation of measurement uncertainties and error propagation of the rotor equivalent wind speed

Some uncertainties from the scanning lidar wind speed measurements, such as the pitch and roll movement of the devices, can be directly accounted for by applying correction algorithms. Others, such as the uncertainty of the measured line-of-sight velocity v_{LOS} or estimated density $\rho(z)$, cannot. To perform an uncertainty estimation concerning these measurements we use Gaussian error propagation on the REWS defined in Equation 11. The total uncertainty of the REWS

$$\Delta v_{\mathrm{eq}} = \sqrt{\sum_i \left(\frac{\partial v_{\mathrm{eq}}}{\partial v_{i,\mathrm{corr}}} \Delta v_{i,\mathrm{corr}}\right)^2 + \sum_i \left(\frac{\partial v_{\mathrm{eq}}}{\partial \phi_i} \Delta \phi_i\right)^2} \tag{B1}$$

is thus calculated as the square root of the sum of squares of the individual uncertainty contributions, with the partial derivatives

$$\frac{\partial v_{\mathrm{eq}}}{\partial v_{i,\mathrm{corr}}} = \left(\sum_i \left((v_{i,\mathrm{corr}} \cos(\phi_i))^3 \frac{A_i}{A_{\mathrm{tot}}}\right)\right)^{-2/3} \cdot v_{i,\mathrm{corr}} \cos(\phi_i)^3 \frac{A_i}{A_{\mathrm{tot}}} \tag{B2}$$

$$\frac{\partial v_{\mathrm{eq}}}{\partial \phi_i} = -\left(\sum_i \left((v_{i,\mathrm{corr}} \cos(\phi_i))^3 \frac{A_i}{A_{\mathrm{tot}}}\right)\right)^{-2/3} \cdot v_{i,\mathrm{corr}}^2 \cos(\phi_i)^2 \sin(\phi_i) \frac{A_i}{A_{\mathrm{tot}}}. \tag{B3}$$

The uncertainty in wind direction difference $\Delta\phi_i$ is assumed to be 1° according to Schneemann et al. (2021). The uncertainty of the density-corrected wind speed, however, is composed of the uncertainty of the measurement itself as well as the computed density. Thus the combined uncertainty reads

$$\Delta v_{i,\mathrm{corr}} = \sqrt{\left(\frac{\partial v_{i,\mathrm{corr}}}{\partial v_i} \cdot \Delta v_i\right)^2 + \left(\frac{\partial v_{i,\mathrm{corr}}}{\partial \rho} \cdot \Delta \rho\right)^2} \tag{B4}$$

with

$$R \frac{\partial v_{\mathrm{i,corr}}}{\partial v_i} = \left(\frac{\rho(z)}{\rho_0}\right)^{1/3} \quad \text{and} \quad \frac{\partial v_{i,\mathrm{corr}}}{\partial \rho} = \frac{1}{3} v_i \rho(z)^{-2/3} {\rho_0}^{-1/3}. \tag{B5}$$

Following Schneemann et al. (2021) we assume an uncertainty of the wind speed of $\Delta v_i = \pm 0.1\,\mathrm{ms}^{-1}$. The Gaussian propagated uncertainty for the density reads as

$$\Delta \rho = \sqrt{\left(\frac{\partial \rho}{\partial T} \Delta T\right)^2 + \left(\frac{\partial \rho}{\partial p} \Delta p\right)^2 + \left(\frac{\partial \rho}{\partial \Phi} \Delta \Phi\right)^2} \tag{B6}$$

with

$$\frac{\partial \rho}{\partial T} = -\frac{1}{T^2}\left(\frac{p(z)}{R_0} - \Phi P_{\mathrm{W}}\left(\frac{1}{R_0} - \frac{1}{R_{\mathrm{W}}}\right)\right), \tag{B7}$$

$$\frac{\partial \rho}{\partial p} = \frac{1}{RT} \quad \text{and} \tag{B8}$$

$$\frac{\partial \rho}{\partial \Phi} = \frac{P_{\mathrm{W}}}{T}\left(\frac{1}{R_0} - \frac{1}{R_{\mathrm{W}}}\right). \tag{B9}$$

For the humidity measurements an uncertainty of $\Delta\Phi = \pm 1\,\%$ is specified. As the height dependent temperature is obtained via the assumption of a simple linear decrease, the uncertainty is specified as $\Delta T(z) = \Delta T_0 = \pm 0.4\,^{\circ}\mathrm{C}$. The height corrected pressure, however, is dependent on the pressure and temperature measured at the transition piece. Hence, its uncertainty is again obtained via Gaussian error propagation as

$$\Delta p(z) = \sqrt{\left(\frac{\partial p(z)}{\partial p_0}\Delta p_0\right)^2 + \left(\frac{\partial p(z)}{\partial T_0}\Delta T_0\right)^2} \tag{B10}$$

with

$$\frac{\partial p(z)}{\partial p_0} = \left(\left(1 + \frac{L}{T_0}\right)(z - z_0)\right)^{g/LR_0} \tag{B11}$$

$$\frac{\partial p(z)}{\partial T_0} = -\frac{L}{T_0^2}\frac{g p_0}{(1 + L/T_0)R_0}\left((z - z_0)\left(\frac{L}{T_0} + 1\right)\right)^{-g/LR_0} \tag{B12}$$

and the measurement uncertainties $\Delta T_0 = \pm 0.4\,^{\circ}\mathrm{C}$ and $\Delta p_0 = \pm 0.1\,\mathrm{hPa}$.

Appendix C: Vertical wind profiles derived from long range lidar PPI scans

Standard profiling lidars typically use conical VAD or DBS scans, with an elevation angle of usually 60°. Here, either single beams in the different cardinal directions or an entire cone is scanned. Wind speed and direction are determined either analytically from the single beam directions (DBS) or via a cosine fit (VAD) (Werner, 2005). The latter method of applying a cosine fit for wind direction estimation and subsequent computation of the horizontal wind speed from the measured line-of-sight wind speeds can also be applied for low-elevation PPI scans (cf. Eq. 4 and e.g. Schneemann et al. (2020)).

To obtain averaged vertical wind profiles for LLJ detection we use the entire lidar scanning volume spanned by the multi-elevation PPI scans. The applied VAD algorithm assumes a horizontally homogeneous wind direction for each range gate of the PPI scans. Local variations in the wind direction can not be resolved by the fit and we obtain a "fit-averaged" wind direction. Since we are working on a time scale of ten minutes (600 s), we are not interested in the small scale dynamics of an inhomogeneous wind field but in the average vertical wind profile representative for the Nordergründe location. The approach to use data from a large measurement volume will inherently produce a mean wind profile in the regarded area, to capture effects persisting on a wind farm scale.

To test how well the volumetric profiles compare to more locally derived wind profiles, we carry out a comparison study. Here it is important to note, that the reconstruction of the horizontal wind speed per range gate is not changed compared to Section 2.2, only the data points which are considered for the wind profile generation are varied between the approaches, i.e. less range gates are included. This also implies, that little changes regarding the derived wind direction occur when reducing the points for generating local vertical wind profiles.

Figure C1 shows the scanning characteristics of the lidar measurements as well as the points on which we generate local vertical wind profiles (virtual met mast, VMast). We position three VMasts inside the measurement volume at distances d of

3 km, 5 km and 7 km from the lidar respectively. For each of the analysed scans, the VMasts are placed along the centre line of the covered azimuth range. Figure C1b shows the exemplary positioning on the centreline of the entire visible sector. In the lidar measurements, however, their positions change due to the varied azimuth angles for each scan being adapted based on the prevailing wind direction. To generate vertical wind profiles at the VMast positions, we include all measurements within a radius $r = 500\,\mathrm{m}$ around the selected location and subsequently average them in vertical bins with a height of 10 m, up to the maximum measurement height at that distance. Subsequently, the generated profiles are resampled to 10-minute averages.

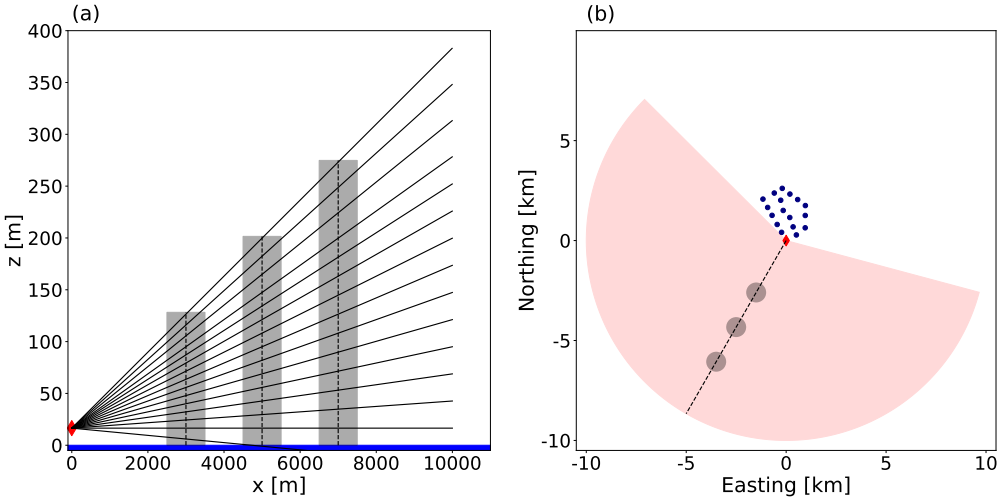

Figure C1. Scanning characteristics of the measurement campaign. (a) Different elevations across the entire range of the scans (black). Relative locations of the VMasts in the scan (dashed lines) and the area of included measurement points for each VMast (grey shaded). The x-axis is oriented along the dashed line in (b). (b) Top view on the measurement sector, with the entire measurement range of the lidar (red) and the sub-areas considered for the VMast approach (grey).

After generating the profiles for the VMast positions and resampling to 10-minute intervals, we compare them to the volumetric profiles (cf. Section 2.2). Due to the smaller volumes available for the data gathering in the VMast approach, the number of available profiles is significantly lower compared to the volumetric approach. The number of valid profiles dropped by 69.5 %, 71.2 % and 75.0 % for the VMasts at 3 km, 5 km and 7 km, respectively.

Figure C2 presents the availability of the retrieved wind profiles across all observed heights. Here, also clear differences between the approaches are observed. While the maximum achievable height increases with distance from the lidar, the overall availability of data points at different heights decreases towards further distances. A clear discrepancy is also visible for the availability compared to the volumetric approach. Here, a significantly increased number of measurements is available across all heights, allowing for a more statistically sound analysis of LLJ appearances at the observed location.

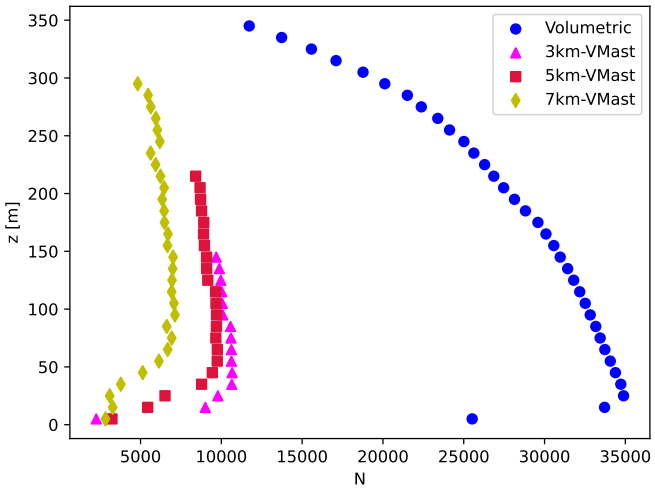

Figure C2. Number of available data points (N) throughout the entire measurement campaign at each height for the different profile generation approaches.

To analyse how well the different profile generation approaches compare against each other, we compute the correlation coefficients between the volumetric wind profiles and the wind profiles derived for each of the three VMasts.

Figure C3 depicts the Pearson correlation coefficient (R^2) between the volumetric profiles and the mast profiles. We observe a high correlation with $R^2 > 0.9$ for all distances at all heights. For the VMasts at 3 km and 5 km the correlation coefficient never drops below 0.95, except for the lowest height level in the 5 km-VMast wind correlation.

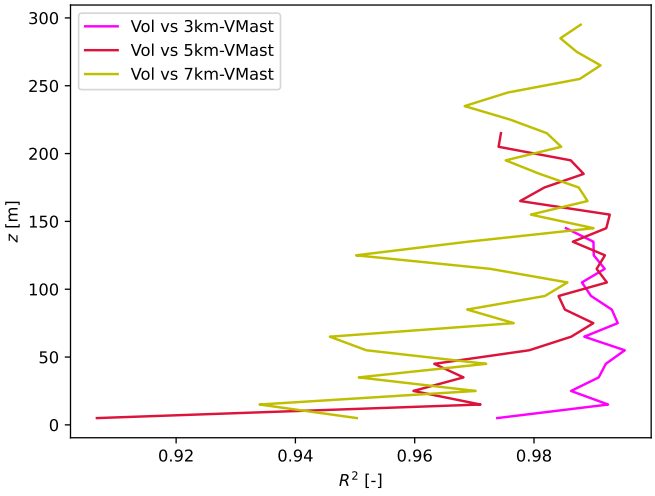

Figure C3. Pearson correlation coefficient between the volumetric and VMast profiles over height.

For a more robust comparison, we also separate the lidar measurements into sea and land sectors, respectively. Here, again very little differences are visible between the wind directions.

Figure C4 shows the correlation coefficients for the different VMast ranges and land and sea sectors respectively. Here, we observe that the correlation coefficients are again very high independently of the prevailing wind direction.

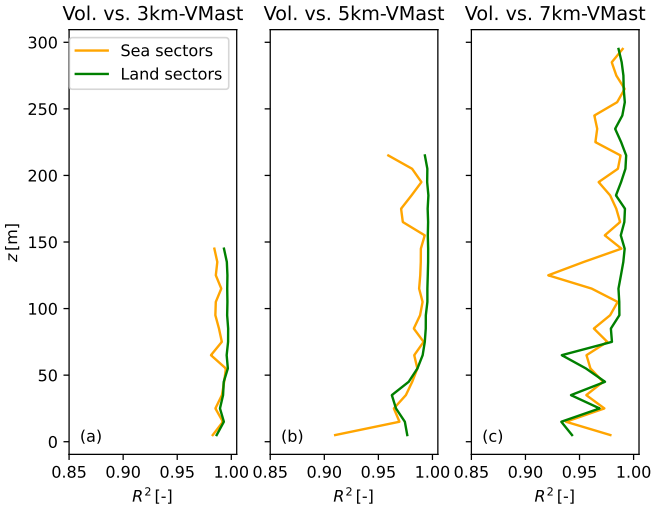

Figure C4. Same as Fig. C3, but separated into land and sea sectors for the VMasts at (a) 3 km, (b) 5 km and (c) 7 km distance to the lidar.

To quantify the fluctuation of wind speeds within a profile we compute the standard deviation of the vertical wind shear. High standard deviations imply strong fluctuations of the shear around the mean shear and hence also strong fluctuations of the wind speed with height. For the volumetric profiles, we observe an average standard deviation of the wind shear of $\overline{\sigma_{\Delta u_i}} = 0.27\,\mathrm{s}^{-1}$. While the standard deviation of the shear decreases very slightly for the 3 km-VMast ($\overline{\sigma_{\Delta u_i}} = 0.26\,\mathrm{s}^{-1}$) a strong increase is observed towards the 5 km-VMast ($\overline{\sigma_{\Delta u_i}} = 0.38\,\mathrm{s}^{-1}$) and even more for the 7 km-VMast ($\overline{\sigma_{\Delta u_i}} = 0.52\,\mathrm{s}^{-1}$).

Finally, we also compare the hub height wind speeds and directions from the volumetric wind profiles to nacelle anemometer measurements from the turbine NG17. To ensure only valid data is included, we again filter for normal operation (cf. Sec. 2.4).

Figure C5 shows scatter plots for the wind speed and wind direction data, respectively, that are obtained from the SCADA system and our volumetric LIDAR approach. These plots include also the regression line. We observe a very high correlation for both wind speed and direction, showing good accordance between the different measurements.

The results from our comparison study suggest, that the volumetric wind profiles we use in our study are in good accordance with more localised wind profiles obtained at different VMast locations as well as nacelle measurements from NG17. The availability of profiles, however, drops significantly with the more localised approach, as well as the quality of the profiles, as fluctuations of the wind speed with height increase. Further, we observe, that the volumetric profiles show highest correlation

to the profiles at d=3 km, i.e. the profiles obtained closest to the wind farm. Here, further development of the profiles towards the farm is lowest.

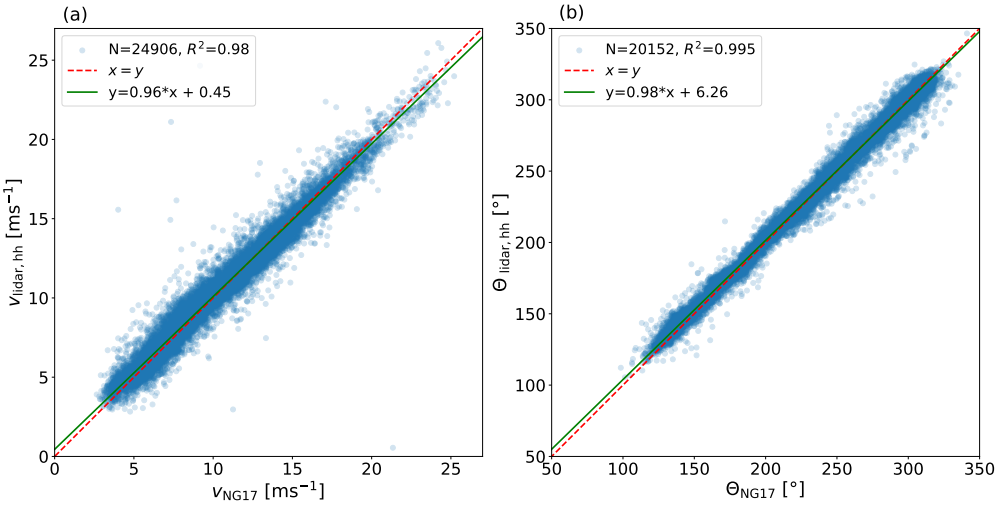

Figure C5. Scatter plot between (a) nacelle wind speed measurements of NG17 lidar derived hub-height wind speed and (b) nacelle measurements of the wind direction and the lidar estimated wind direction at hub height. The dashed red line shows the $x = y$ and the regression line is drawn in green.

Author contributions. JP conducted the main research and wrote the majority of the manuscript. JS planned, conducted, executed and supervised the measurement campaign, provided extensive feedback on the data analysis and the manuscript, contributed to the scientific discussion and wrote the majority of Appendix A. GS provided significant feedback in reviewing the manuscript and on the data analysis and significantly contributed to the scientific discussion. FT supervised the measurement campaign, provided support by reviewing the manuscript and contributed to the scientific discussion. MK supervised the work, contributed to the scientific discussion and provided significant feedback in reviewing the manuscript.

Competing interests. The authors declare no competing interests.

Acknowledgements. We thank the wind farm operator OWP Nordergründe GmbH & Co. KG for providing operational data of the wind farm Nordergründe and their great support of our measurement campaign.

We thank Marcos Ortensi and Richard Frühmann for their help with the IR-SST measurements. We acknowledge the data provision of Wasserstraßen- und Schifffahrtsamt Weser-Jade-Nordsee and their support of our measurement campaign in the WindRamp project.

The measurements and parts of the work have been funded by the German Federal Ministry for Economic Affairs and Energy on the basis of a decision by the German Bundestag (research projects "X-Wakes" (FKZ 03EE3008D), "WindRamp" (FKZ 03EE3027A) and "C^2-Wakes" (FKZ 03EE3087B)). Parts of the work have been funded by the EU project FLOW within the European Union Horizon Europe Framework programme (HORIZON-CL5-2021-D3-03-04) under grant agreement no. 101084205. Johannes Paulsen is supported by the Deutsche Bundesstiftung Umwelt (grant no. 20022/047).

References

Aird, J. A., Barthelmie, R. J., Shepherd, T. J., and Pryor, S. C.: Occurrence of Low-Level Jets over the Eastern U.S. Coastal Zone at Heights Relevant to Wind Energy, Energies, 15, https://doi.org/10.3390/en15020445, 2022.

Baas, P., Bosveld, F. C., Klein Baltink, H., and Holtslag, A. A. M.: A Climatology of Nocturnal Low-Level Jets at Cabauw, Journal of Applied Meteorology and Climatology, 48, 1627–1642, https://doi.org/10.1175/2009JAMC1965.1, 2009.

Baki, H., Basu, S., and Lavidas, G.: Modeling Frontal Low-Level Jets and Associated Extreme Wind Power Ramps over the North Sea, Wind Energy Science, 10, 1575–1609, https://doi.org/10.5194/wes-10-1575-2025, 2025.

Barekzai, M., Cañadillas, B., Emeis, S., Dörenkämper, M., and Lampert, A.: Mesoscale simulations of coastal boundary-layer transitions. Part 2: offshore wind speed development, Meteorologische Zeitschrift, 33, 475, https://doi.org/10.1127/metz/2024/1196, 2025a.

Barekzai, M., Cañadillas, B., Emeis, S., Dörenkämper, M., and Lampert, A.: Mesoscale simulations of coastal boundary-layer transitions. Part 1: low-level jets, Meteorologische Zeitschrift, 33, 457, https://doi.org/10.1127/metz/2024/1195, 2025b.

Browning, K. A. and Harrold, T. W.: Air Motion and Precipitation Growth at a Cold Front, Quarterly Journal of the Royal Meteorological Society, 96, 369–389, https://doi.org/10.1002/qj.49709640903, 1970.

Bui, H., Bakhoday-Paskyabi, M., and Reuder, J.: Characterization and Bias-Correction of Low-Level Jets at FINO1 Using LiDAR Observations and Reanalysis Data, https://doi.org/10.5194/wes-2025-91, 2025.

Cañadillas, B., Beckenbauer, M., Trujillo, J. J., Dörenkämper, M., Foreman, R., Neumann, T., and Lampert, A.: Offshore Wind Farm Cluster Wakes as Observed by Long-Range-Scanning Wind Lidar Measurements and Mesoscale Modeling, Wind Energy Science, 7, 1241–1262, https://doi.org/10.5194/wes-7-1241-2022, 2022.

Dörenkämper, M., Tambke, J., Steinfeld, G., Heinemann, D., and Kühn, M.: Atmospheric Impacts on Power Curves of Multi-Megawatt Offshore Wind Turbines, Journal of Physics: Conference Series, 555, 012 029, https://doi.org/10.1088/1742-6596/555/1/012029, 2014.

Dörenkämper, M., Optis, M., Monahan, A., and Steinfeld, G.: On the Offshore Advection of Boundary-Layer Structures and the Influence on Offshore Wind Conditions, Boundary-Layer Meteorology, 155, 459–482, https://doi.org/10.1007/s10546-015-0008-x, 2015.

Emeis, S.: Wind Speed and Shear Associated with Low-Level Jets over Northern Germany, Meteorologische Zeitschrift, 23, 295–304, https://doi.org/10.1127/0941-2948/2014/0551, 2014.

Emeis, S.: Wind Energy Meteorology, Green Energy and Technology, Springer International Publishing, Cham, https://doi.org/10.1007/978-3-319-72859-9, 2018.

Gadde, S. N. and Stevens, R. J. A. M.: Interaction between Low-Level Jets and Wind Farms in a Stable Atmospheric Boundary Layer, Physical Review Fluids, 6, 014 603, https://doi.org/10.1103/PhysRevFluids.6.014603, 2021.

Goit, J. P., Yamaguchi, A., and Ishihara, T.: Measurement and Prediction of Wind Fields at an Offshore Site by Scanning Doppler LiDAR and WRF, Atmosphere, 11, 442, https://doi.org/10.3390/atmos11050442, 2020.

Good, S., Fiedler, E., Mao, C., Martin, M. J., Maycock, A., Reid, R., Roberts-Jones, J., Searle, T., Waters, J., While, J., and Worsfold, M.: The Current Configuration of the OSTIA System for Operational Production of Foundation Sea Surface Temperature and Ice Concentration Analyses, Remote Sensing, 12, 720, https://doi.org/10.3390/rs12040720, 2020.

Guest, P., Persson, P. O. G., Wang, S., Jordan, M., Jin, Y., Blomquist, B., and Fairall, C.: Low-Level Baroclinic Jets Over the New Arctic Ocean, Journal of Geophysical Research: Oceans, 123, 4074–4091, https://doi.org/https://doi.org/10.1002/2018JC013778, 2018.

Gutierrez, W., Ruiz-Columbie, A., Tutkun, M., and Castillo, L.: Impacts of the Low-Level Jet's Negative Wind Shear on the Wind Turbine, Wind Energy Science, 2, 533–545, https://doi.org/10.5194/wes-2-533-2017, 2017.

Hallgren, C., Aird, J. A., Ivanell, S., Körnich, H., Barthelmie, R. J., Pryor, S. C., and Sahlée, E.: Brief communication: On the definition of the low-level jet, Wind Energy Science, 8, 1651–1658, https://doi.org/10.5194/wes-8-1651-2023, 2023.

IEC: IEC 61400-12-1:2017 - Wind energy generation systems - Part 12-1: Power performance measurements of electricity producing wind turbines, Tech. rep., IEC, 2017.

Jonkman, B. J. and Buhl, Jr., M. L.: TurbSim User's Guide, Tech. Rep. NREL/TP-500-36970, 15020326, National Renewable Energy Lab. (NREL), https://doi.org/10.2172/15020326, 2005.

Jonkman, J., Butterfield, S., Musial, W., and Scott, G.: Definition of a 5-MW Reference Wind Turbine for Offshore System Development, Tech. Rep. NREL/TP-500-38060, 947422, National Renewable Energy Lab. (NREL), https://doi.org/10.2172/947422, 2009.

Kalverla, P. C., Duncan Jr., J. B., Steeneveld, G.-J., and Holtslag, A. A. M.: Low-Level Jets over the North Sea Based on ERA5 and Observations: Together They Do Better, Wind Energy Science, 4, 193–209, https://doi.org/10.5194/wes-4-193-2019, 2019.

Lampert, A., Bernalte Jimenez, B., Gross, G., Wulff, D., and Kenull, T.: One-Year Observations of the Wind Distribution and Low-Level Jet Occurrence at Braunschweig, North German Plain: Wind Distribution and Low-Level Jet Occurrence at Braunschweig, Wind Energy, 19(10), 1807–1817, https://doi.org/10.1002/we.1951, 2016.

Lopez-Villalobos, C. A., Martínez-Alvarado, O., Rodriguez-Hernandez, O., and Romero-Centeno, R.: Analysis of the Influence of the Wind Speed Profile on Wind Power Production, Energy Reports, 8, 8079–8092, https://doi.org/10.1016/j.egyr.2022.06.046, 2022.

Mittelmeier, N., Allin, J., Blodau, T., Trabucchi, D., Steinfeld, G., Rott, A., and Kühn, M.: An Analysis of Offshore Wind Farm SCADA Measurements to Identify Key Parameters Influencing the Magnitude of Wake Effects, Wind Energy Science, 2, 477–490, https://doi.org/10.5194/wes-2-477-2017, 2017.

Mortarini, L., Cava, D., Giostra, U., Acevedo, O., Nogueira Martins, L., Soares de Oliveira, P. E., and Anfossi, D.: Observations of Submeso Motions and Intermittent Turbulent Mixing across a Low Level Jet with a 132-m Tower, Quarterly Journal of the Royal Meteorological Society, 144, 172–183, https://doi.org/10.1002/qj.3192, 2018.

Murphy, P., Lundquist, J. K., and Fleming, P.: How Wind Speed Shear and Directional Veer Affect the Power Production of a Megawatt-Scale Operational Wind Turbine, Wind Energy Science, 5, 1169–1190, https://doi.org/10.5194/wes-5-1169-2020, 2020.

National Renewable Energy Laboratory: OpenFAST v3.5.0, https://github.com/OpenFAST/openfast, last Access: 2025-05-07., 2023.

Ohya, Y., Nakamura, R., and Uchida, T.: Intermittent Bursting of Turbulence in a Stable Boundary Layer with Low-level Jet, Boundary-Layer Meteorology, 126, 349–363, https://doi.org/10.1007/s10546-007-9245-y, 2008.

Olsen, B. T. E., Hahmann, A. N., Alonso-de-Linaje, N. G., Žagar, M., and Dörenkämper, M.: Low-Level Jets in the North and Baltic Seas: Mesoscale Model Sensitivity and Climatology Using WRF V4.2.1, Geoscientific Model Development, 18, 4499–4533, https://doi.org/10.5194/gmd-18-4499-2025, 2025.

Osterman, A.: Implementation of the r. Cuda. Los Module in the Open Source GRASS GIS by Using Parallel Computation on the NVIDIA CUDA Graphic Cards, Elektrotehniski Vestnik/Electrotechnical Review, 79(1), 19–24, https://ev.fe.uni-lj.si/1-2-2012/Osterman.pdf, 2012.

Pichugina, Y. L., Brewer, W. A., Banta, R. M., Choukulkar, A., Clack, C. T. M., Marquis, M. C., McCarty, B. J., Weickmann, A. M., Sandberg, S. P., Marchbanks, R. D., and Hardesty, R. M.: Properties of the offshore low level jet and rotor layer wind shear as measured by scanning Doppler Lidar, Wind Energy, 20, 987–1002, https://doi.org/https://doi.org/10.1002/we.2075, 2017.

Ranjha, R., Svensson, G., Tjernström, M., and Semedo, A.: Global Distribution and Seasonal Variability of Coastal Low-Level Jets Derived from ERA-Interim Reanalysis, Tellus A: Dynamic Meteorology and Oceanography, 65, 20412, https://doi.org/10.3402/tellusa.v65i0.20412, 2013.

Rausch, T., Cañadillas, B., Hampel, O., Simsek, T., Tayfun, Y. B., Neumann, T., Siedersleben, S., and Lampert, A.: Wind Lidar and Radiosonde Measurements of Low-Level Jets in Coastal Areas of the German Bight, Atmosphere, 13, 839, https://doi.org/10.3390/atmos13050839, 2022.

Rott, A., Schneemann, J., Theuer, F., Trujillo Quintero, J. J., and Kühn, M.: Alignment of scanning lidars in offshore wind farms, Wind Energy Science, 7, 283–297, https://doi.org/10.5194/wes-7-283-2022, 2022.

Roy, S., Sentchev, A., Fourmentin, M., and Augustin, P.: Machine Learning and Deterministic Methods for Detection Meteorological Phenomena from Ground Measurements: Application for Low-Level Jet and Sea-Breeze Identification in Northern France, Atmosphere, 13, 1873, https://doi.org/10.3390/atmos13111873, 2022.

Rubio, H., Kühn, M., and Gottschall, J.: Evaluation of low-level jets in the southern Baltic Sea: a comparison between ship-based lidar observational data and numerical models, Wind Energy Science, 7, 2433–2455, https://doi.org/10.5194/wes-7-2433-2022, 2022.

Sathe, A., Mann, J., Gottschall, J., and Courtney, M.: Estimating the Systematic Errors in Turbulence Sensed by Wind Lidars, Tech. rep., Risø National Laboratory, Roskilde, Denmark, https://www.academia.edu/45626721/Estimating_the_systematic_errors_in_turbulence_sensed_by_wind_LIDARs, last Access: 2024-10-04, 2022.

Schepers, G., Dorp, P. V., Verzijlbergh, R., Baas, P., and Jonker, H.: Aeroelastic loads on a 10 MW turbine exposed to extreme events selected from a year-long large-eddy simulation over the North Sea, Wind Energy Science, 6, 983–996, https://doi.org/10.5194/wes-6-983-2021, 2021.

Schneemann, J., Rott, A., Dörenkämper, M., Steinfeld, G., and Kühn, M.: Cluster Wakes Impact on a Far-Distant Offshore Wind Farm's Power, Wind Energy Science, 5, 29–49, https://doi.org/10.5194/wes-5-29-2020, 2020.

Schneemann, J., Theuer, F., Rott, A., Dörenkämper, M., and Kühn, M.: Offshore Wind Farm Global Blockage Measured with Scanning Lidar, Wind Energy Science, 6, 521–538, https://doi.org/10.5194/wes-6-521-2021, 2021.

Schulz-Stellenfleth, J., Emeis, S., Dörenkämper, M., Bange, J., Cañadillas, B., Neumann, T., Schneemann, J., Weber, I., zum Berge, K., Platis, A., Djath, B., Gottschall, J., Vollmer, L., Rausch, T., Barekzai, M., Hammel, J., Steinfeld, G., and Lampert, A.: Coastal Impacts on Offshore Wind Farms – a Review Focussing on the German Bight Area, Meteorologische Zeitschrift, 31, 289–315, https://doi.org/10.1127/metz/2022/1109, 2022.

St. Martin, C. M., Lundquist, J. K., Clifton, A., Poulos, G. S., and Schreck, S. J.: Wind Turbine Power Production and Annual Energy Production Depend on Atmospheric Stability and Turbulence, Wind Energy Science, 1, 221–236, https://doi.org/10.5194/wes-1-221-2016, 2016.

Theuer, F., Seifert, J. K., Schneemann, J., and Kühn, M.: Enhancing Minute-Scale Lidar-Based Power Forecasts of Offshore Wind Farms towards an Operational Use, Wind Energy Science Discussions, pp. 1–27, https://doi.org/10.5194/wes-2024-141, 2024.

Visich, A. and Conan, B.: Measurement and Analysis of High Altitude Wind Profiles over the Sea in a Coastal Zone Using a Scanning Doppler LiDAR: Application to Offshore Wind Energy, Ocean Engineering, 325, 120 749, https://doi.org/10.1016/j.oceaneng.2025.120749, 2025.

Wagner, D., Steinfeld, G., Witha, B., Wurps, H., and Reuder, J.: Low Level Jets over the Southern North Sea, Meteorologische Zeitschrift, 28, 389–415, https://doi.org/10.1127/metz/2019/0948, 2019.

Weide Luiz, E. and Fiedler, S.: Spatiotemporal Observations of Nocturnal Low-Level Jets and Impacts on Wind Power Production, Wind Energy Science, 7, 1575–1591, https://doi.org/10.5194/wes-7-1575-2022, 2022.

Werner, C.: Doppler Wind Lidar, in: Lidar, edited by Weitkamp, C., vol. 102, pp. 325–354, Springer-Verlag, New York, https://doi.org/10.1007/0-387-25101-4_12, 2005.

WSV: PegelOnline, https://www.pegelonline.wsv.de, last access: 2025-05-07., 2023.

Zhang, X., Yang, C., and Li, S.: Influence of the Heights of Low-Level Jets on Power and Aerodynamic Loads of a Horizontal Axis Wind Turbine Rotor, Atmosphere, 10, 132, https://doi.org/10.3390/atmos10030132, 2019.